COMPUTATIONAL MODELING OF MAXIMUM LENGTH SEQUENCE (MLS) MULTILAYER AND GRATING STRUCTURES

by

Khem Narayan Poudel

A Dissertation

Presented to the Faculty of the Computational Science Program

Middle Tennessee State University

February 2020

In Partial Fulfillment

of the Requirements for the Degree

Doctorate of Philosophy in Computational Sciences

Dissertation Committee:

Dr. William M. Robertson, Chair

Dr. Zachariah Sinkala

Dr. Qiang Wu

Dr. Yating Hu

To my parents, adorable wife and daughters.

ACKNOWLEDGMENTS

First and foremost I would like to express my sincere gratitude to my advisor Prof. Dr. William M. Robertson, for the continuous support of my Ph.D study and research, for his motivation, patience, and immense knowledge. I could not have imagined having a better advisor and mentor for my PhD study. I am very grateful to him for introducing me to the new concept of maximum length sequences and Bloch surface waves and advising me to get into depth part of it.

I would like to thank the rest of my thesis committee: Dr. Zachariah Sinkala, Dr. Qiang Wu, and Dr. Yating Hu for their insightful comments and encouragement on my dissertation.

I would like to thank Middle Tennessee State University and the Computational Science program for funding my graduate studies and research. My sincere thanks also goes to Dr. John F. Wallin for his full support throughout my PhD program and who has support me each and every academic success and through difficult times. I would like to thank the Physics and Astronomy department chair, Dr. Ronald Henderson and the Computer Science department chair Dr. Medha Sarkar for their full support throughout my PhD program.
I am grateful to to all the faculty members and staff of the Computational Science Program and Physics and Astronomy department, Computer Science Department along with my friends for helping me in any means. Last but not the least, I would like to thank my parents, my loving and supportive wife, Pratima, and my two wonderful daughters, Prajna, and Prisca who provide unending support and inspiration.

ABSTRACT

This thesis describes a variety of projects computing the optical response of periodic and aperiodic structures. The projects include the design of dielectric multilayer, grating, frequency selective surface and antennas, Mostly, this explores the wavelength-dependent reflectivity of alternating high and low refractive index multilayers with a thickness profile defined by a pseudo-random, maximum length sequence (MLS). An MLS contains all possible combinations of a binary sequence save one; thus, a multilayer with an MLS profile contains a superposition of a broad range of periods. The range of periodicities in an MLS multilayer should make these systems more effective broad wavelength reflectors as compared to purely periodic counterparts. We compute the reflection characteristics of MLS and periodic dielectric sequences at visible wavelengths over a range of incident angles using the transfer matrix method (TMM), a recursive multilayer calculation method. The materials SiO_2 and TiO_2 are chosen as the low and high refractive index materials, respectively, because these materials are commonly used in optical multilayers and because their wavelength-dependent refractive index is well known. Our results show that it is possible to create an MLS structure with high average reflectivity across the entire visible spectrum (400 nm - 700 nm) at all incident angles and polarizations. Finally, we compare the reflection characteristics of dielectric multilayers with metallic reflectors whose refractive index is based on a Brendel-Bormann (BB) model.The comparison shows that a seventh order MLS aperiodic multilayer exhibits slightly higher average reflectivity over the visible spectum than silver or aluminum metallic reflectors.

The study of Bloch surface waves (BSWs) in dielectric multilayers has been useful in many applications in the fields of optics, photonics, and bio-sensing. BSW excitation can be achieved by the addition of a grating on the top of dielectric multilayer which provides phase matching between incident light and BSWs. However, grating coupling only provides coupling over a narrow angular range for incident monochromatic radiation. This paper reports work on realizing broadband coupling using maximum length sequence (MLS) grating

structures. An MLS grating contains all possible combinations of a binary sequence save one; thus a grating with an MLS profile contains a superposition of a broad range of periods. We hypothesize that such a surface structure will permit coupling of a broad angular range of monochromatic light or a wide spectral range of collimated light into Bloch surface wave on a multilayer. We investigate the comparative spectral characteristics of MLS grating coupling with other single period counterparts. We believe our investigation provides a method to achieve efficient coupling of a higher fraction of incident light into BSWs than a single period grating or by using prism coupling.

We analyze periodic arrays of frequency selective surfaces (FSS_s) built from the split ring resonators (SRR_s) and $CSRRs$. FSSs are two-dimensional periodic structures that behave like either passband or stop band filters in the microwave frequency band. SRRs are artificially created structures with non-magnetic loops and small gaps between them. Using COMSOL Multi-physics, we investigate the transmission characteristics of such structures with variation of the physical parameters gap width, dielectric constant, gap separation, and incident angle. This analysis offers a new approach in the design of meta-material based radio frequency(RF) devices.

We present a metamaterial-based design of large scale antennas for massive multiple input and multiple output (MIMO) communication systems. The reliable data link and better performance over modern fifth generation (5G) wireless communication systems is possible with large numbers of such adaptive antennas. The miniature metamaterial antennas are best for practical implementation of such large antenna arrays. We investigate the design of metamaterial antennas and analyze the S-parameter, radiation pattern, and define mathematical relationship to find the correlation coefficient and diversity gain.

TABLE OF CONTENTS

LIST OF TABLES

LIST OF FIGURES

CHAPTER 1

INTRODUCTION

In this thesis the interaction of light with materials with an aperiodic index profile is examined. We are mainly interested on two major goals, the design of omnidirectional reflector and a surface grating capable of broadband coupling of light to surface and guided waves. The specific aperiodic profile is the maximal length sequence(MLS. An MLS contains all possible combinations of a binary sequences save one; and it has a uniformly flat frequency response except for a DC offset. The aperiodic index profile is studied here in two forms. First, an optical multilayer consisting of alternating layers two different refractive index materials in which the layer thicknesses have an MLS pattern. We explore the feasibility of creating a functional omnidirectional reflector across all wavelengths in the visible without the necessity of materials with extremely high index contrast. Periodic dielectric multilayers act as near perfect reflectors over a limited wavelength and angular range and provide excellent reflectivity, low absorption loss, and a high degree of robustness compared to metallic reflectors [72]. However, periodic dielectric multilayer reflectors are not highly reflective of light coming from any direction and polarization. In general, the range of reflected wavelengths shifts to another wavelength the blue end of the spectrum at angles away from normal incidence. An ideal omnidirectional dielectric multilayer reflector would have near perfect reflection for all wavelengths in a given range and at all incident angles and any polarization. In the visible range, metallic mirrors from materials such as silver and aluminum have such properties [73, 74]. The goal here is to make a metallic-like reflector from a multilayer structure using the deterministically pseudo-random maximum length sequence thickness profile. Our results show that it is possible to create an MLS structure with high average reflectivity across the entire visible spectrum (400 nm - 700 nm) at all incident angles and polarizations. Further, we compare the reflection characteristics of dielectric multilayers with metallic reflectors whose refractive index is based on a Brendel-Bormann

(BB) model.The comparison shows that a seventh order MLS aperiodic multilayer exhibits slightly higher average reflectivity over the visible spectum than silver or aluminum metallic reflectors.

The second major objective is to explorer a surface grating profile which possesses an MLS pattern.We posit that such a MLS grating surface structure will permit coupling of a broad angular range of monochromatic light or a wide spectral range of collimated light into Bloch surface waves on a (PBG) multilayer. We investigate the characteristics of MLS grating coupling by varying material refractive index, incident angle, and operating wavelengths

1.1 Dissertation Objective

Our proposed computational investigation examines the response of optical multilayers consisting of alternating high and low refractive index materials with a thickness profile determined by a pseudo-random maximum length sequence (MLS). The major objectives can be classified as MLS dielectric multilayer reflector design and MLS Bloch surface wave coupling. These objectives are briefly described as

- The first aim of our research is to demonstrate that such multilayers have higher reflectivity over a broader bandwidth than periodic multilayers with the same index contrast and number of layers. For periodic multilayers, the forbidden transmission bandwidth, the photonic band gap of the one dimensional photonic crystal, is set by the index contrast between the two materials. Higher index contrast leads to band gaps with broader frequency coverage. A maximum length sequence (MLS) is a two-level pseudo-random binary sequence which has a uniformly flat frequency response except for a DC offset [1]. The flat frequency response indicates that these sequences contain equal amplitudes of all possible periodicities [2–4]. We posit that a multilayer using a thickness profile determined by an MLS will have a broader range of periods and, hence, will exhibit a wider bandgap than a periodic system of the same materials and number of layers.

- The second objective is to explorer a method of broadband coupling to $BSWs$ using maximum length sequence (MLS) grating structures on the top of multilayer structure. The MLS grating has a superposition of a broad range of periodicities which should permit coupling of a broad angular range of monochromatic light or a wide spectral range of collimated light into Bloch surface wave on a photonic band gap multilayer.

1.2 Multilayers and 1-D Photonic Band Gaps

When electromagnetic waves propagate through a multilayer structure, reflection, refraction, absorption, and interference determine the transmission and reflection. For some particular wavelength of light the multiple reflections from each layer add constructively. In this case the overall reflection of system reaches almost unity and forms a so-called perfect dielectric mirror for that particular wavelength. Such periodic multilayer structures are commonly known as one-dimensional photonic crystals and the range of wavelengths over which the system is highly reflective is called the photonic band gap (PBG). However, such ideal infinitely extended photonic crystals can not exist in reality and we have to truncate. Truncation of the photonic crystal introduces a new electromagnetic mode known as a Bloch surface wave (BSW_s) BSWs are modes that propagate along the interface of a truncated dielectric multilayer structure and a homogeneous medium. The electromagnetic field in the layered media can be expressed as

$$E(z,x,t) = E_K(z)exp(jKz)exp(j(\beta x - \omega t)) \tag{1}$$

where $E_K(z)$ the electric wave amplitude is a periodic function of z. The z axis is normal to the interface and β is the propagation constant in the plane of the multilayer, and K is a complex wave vector that can be expressed as $K = \frac{m\pi}{\Lambda} \pm jK_i$ [5]. Here, Λ is the period of the multilayer and m is an integer. For the finite periodic medium, with a particular wavelength and incident angle, an exponentially decaying wave exists in both external media bounding the interface and the maxuimum electric field exists at the surface. Such modes confined

at the interface of multilayer are called Bloch surface waves. $BSWs$ were predicted and experimentally observed using a prism coupling configuration in SiO_2 and TiO_2 multilayer structures [7,8]. Bloch surface waves on low-loss dielectric stacks act as a promising alternative to surface plamson polaritons $SPPs$ which are a similar surface bound electromagnetic mode on the surface of metals. The advantages of BSWs are due to the flexibility in operating wavelength range, easier experimental realization, larger figure of merit (FOM) for sensing applications, and suitability in many sensing applications. The benefits of $BSWs$ provide a wider ranges of applications such as in photonic integrated circuits [9], label free bio-sensing [10], surface enhanced Raman spectroscopy [11], optical fiber tip sensors [12], radiation continuum modes [13], optical slow light devices [14], florescence based detection [15], and slot waveguides [16].

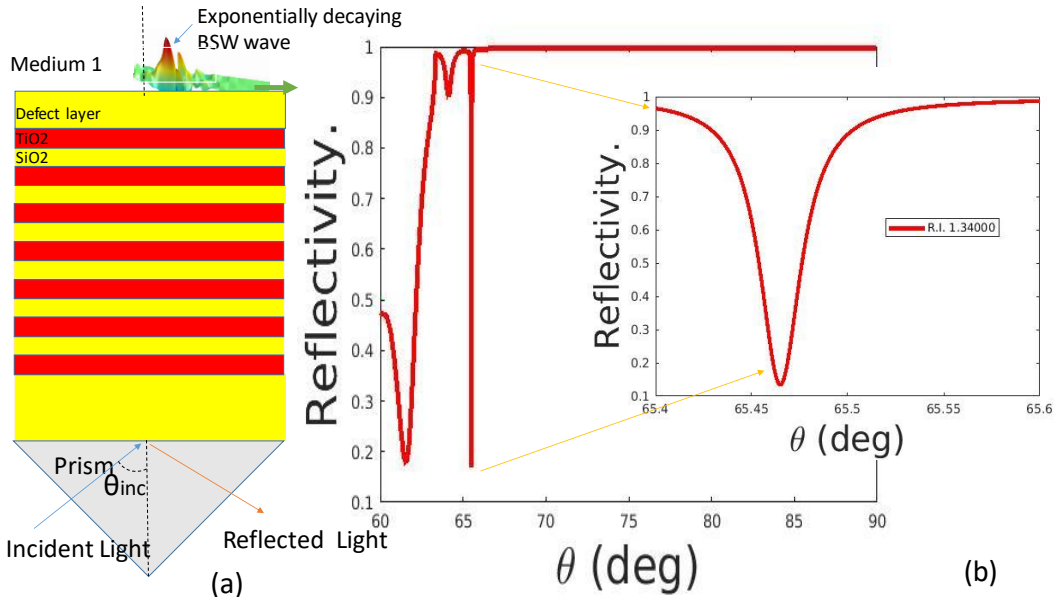

Figure 1: BSW excitation (a) using a prism configuration and (b) The reflection characteristics. The reflectivity dip occurs when light is coupled into a BSW.

Figure 1 shows the BSW excitation using a prism coupling configuration in a multilayer structure design using alternate low and high refractive index materials. The exponentially decaying wave can be observed at the top defect layer of these structure for particular inci-

dent angle and wavelength. Figure 1 (b) shows the reflection characteristics which exhibits a narrow dip at an incident angle of around 66 degrees. The reflectivity dip occurs when the incident light through the prism generates BSWs. These $BSWs$ are non-radiative excitations with larger momentum than light at the same frequency. This momentum mismatch requires some phase-matching mechanism to couple to light. Most methods in are based on surface wave excitation using prism-coupling or a periodic grating structure on the top of the active medium [17]. In both cases, the incident wave is coupled into a surface mode of the structure only when the parallel-wave-vector phase matching condition is satisfied [18]. For the prism multilayer configuration, with no grating, we can express $K_{BSW} = \eta_{prism} \times \frac{2\pi}{\lambda} sin\theta_{res}$. However, this method requires a bulky prism which is not practical for the design of nanoscale optical devices. So, the grating surface at the top of multilayer structure that supports the Bloch surface wave is a desirable alternative to the prism configuration. The wave vector phase matching criterion for grating coupling can be expressed as

$$k_{BSW} = k_0 \eta_{sup} sin(\theta_{inc}) + \frac{2\pi m}{\Lambda_g} \tag{2}$$

where k_{BSW} is BSW wave vector, $k_0 = \frac{2\pi m}{\lambda_0}$ is free space wave vector, η_{sup} is the refractive index of superstrate, θ_{inc} is the incident angle, m is an integer, and Λ is the grating period. For a given wavelength λ, m=1 and $\theta_{inc} > 0$, the BSW can only be excited when the grating period Λ_g satisfies the condition of $\frac{\lambda}{\Lambda} < \frac{k_{BSW}}{k_0} + 1$.Thus the range of grating periods is in the range of $\frac{k_{BSW}}{k_0} < \frac{\lambda}{\Lambda} < \frac{k_{BSW}}{k_0} + 1$. Now, we briefly discuss about the fundamental principle behind the maximum length sequence generation, multilayer impedance formulation, MLS grating design for BSW_s excitation and terahertz time domain system.

1.3 Maximum Length Sequence

The properties of maximum length sequences have been applied in a variety of settings from signal processing, architectural acoustics, and cellular communications [19–22]. In acoustics, the MLS is used to measure impulse response and reverberation-decay inside a room or a

theatre [19]. Higher signal−to−noise ratio (SNR) is possible in a noisy measurement system, as the MLS frequencies are distributed randomly over the entire spectrum. Low noise impulse response at the output is calculated using a cross correlation procedure [21]. Similarly, in wireless communication, using code division multiple access (CDMA), user data is spread independently with MLS (commonly called spread spectrum) over the entire bandwidth at the transmitter side. On the receiver side, the signal is despread using a synchronization replica of the MLS sequence [22].

Maximum length sequences are binary sequences also known as pseudo-random binary sequences (PRBS) that are commonly generated by a cyclic shift of m-sized linear feedback shift registers (LFSR) along with a primitive polynomial. A primitive polynomial is an irreducible polynomial that can produce all the sequences of an extension field from a base field. Figure 2 shows the shift register arrangement for the generation of a 63-element ($N = 2^6 - 1$) long sequence (which, as we show below, corresponds to 32 distinct layers) using 6 LFSR and an XOR gate. Computationally, these sequences can be generated using the recursive formulation $S_{k+3} = S_{k+1} \oplus S_k$. Here, the $\oplus$ symbol represents XOR (modulo-2 sum) operation [1–3].

All MLS sequences produce a flat frequency response. The frequency response for N=6 is illustrated in Figure 2 (b). The MLS exhibits very low values of correlation except at zero offset, a feature that is used in the acoustic impulse and spread spectrum communication applications. Figure 2 shows the flat Fourier spectrum, which is the relevant feature in our applications. This feature shows that all periodicities are equally contained in the sequence.

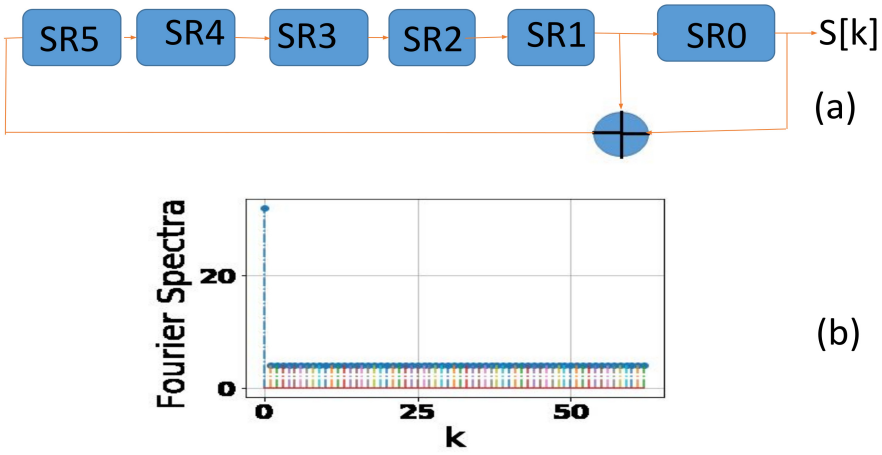

Figure 2: (a) MLS generation using shift registers and an XOR gate. (b) Flat Fourier spectra for 6^{th} order MLS multilayer structure.

To make the generation process clear we present a simple example for the N=3 MLS sequence in Figure 3. The process begins with the seed for N=3 which consists of three elements equal to one. The next element in the sequence is generated by taking the XOR of the first two elements; the taps in this example are at positions 1 and 2. The result $1 \oplus 1 = 0$ is highlighted in blue. The sequence shifts to the left and the fifth element of the sequence is the $\oplus$ of elements 2 and 3. The process continues until the sequence replicates the seed at which point the sequence will repeat. The existence of all periods but one in the generated sequence can be shown by going through the sequence grouping the elements in sets of three. This process shows that every possible permutation of three elements occurs once in the sequence except for [0 0 0]. Each 1 and 0 in the generated sequence represents high and low refractive index materials respectively. Grouping the like elements leads to the values [3 2 1 1] for N=3.To convert this set of values into a multilayer involves selecting a minimum thickness for the high and low index layers d_H and d_L. Typically for the visible reflector we chose $d_H = \lambda/4n_H$ and $d_L = \lambda/4n_L$ where n_H and n_L are the refractive index values of the two materials respectively. The multilayer thicknesses would then be given by $[3d_H\ 2d_L\ 1d_H\ 1d_L]$. For these simulations we chose λ to be 550 nm resulting in high reflectivity across the visible.

Table 1 defines the MLS sequence in terms of order, tap, and number of distinct layers. The 6^{th} order MLS multilayer structure along with taps at 1 and 2 has 32 distinct alternate high and low refractive index materials derived from the 63 sequence elements. As for the simple N=3 case illustrated in Figure 2, to convert the MLS sequence to multilayer thicknesses the 1 and 0 are taken to correspond to the two different refractive index materials. Thus, the final 7 element sequence for N=3 is expressed as [3 2 1 1] with 4 distinct layers. The 6^{th} order MLS multilayer structure thickness is determined by following alternate high and low refractive index sequence: $[6, 5, 1, 4, 2, 3, 1, 1, 1, 2, 4, 1, 1, 3, 3, 2, 1, 2, 1, 1, 2, 1, 3, 1, 2, 2, 2, 1, 1, 1, 1, 1]$. This sequence length is 63 (2^6-1) which converts to 32 distinct high and low index layers.

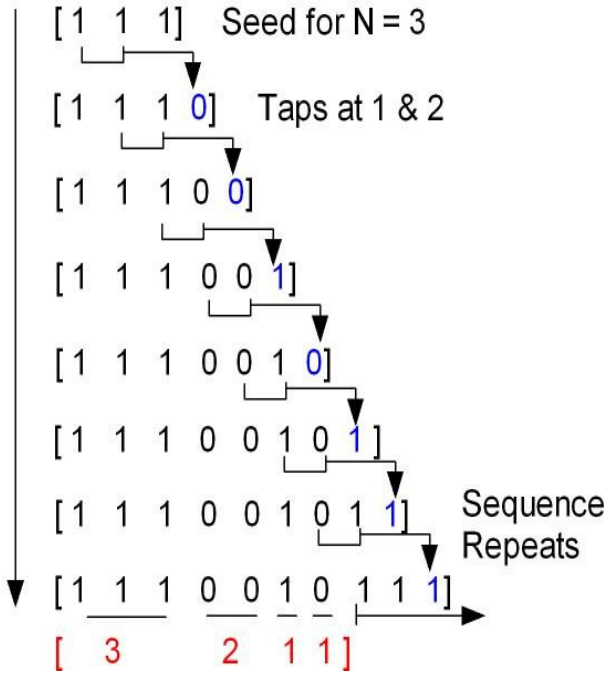

Figure 3: Illustration of the generation process for the N=3 maximal length sequence.

Table 1: Orders of MLS sequence generation

Order(N)	Tap	Sequence	Total single layers	Distinct layers
3	1,2	[3 2 1 1]	7	4
4	1,2	[4 3 1 2 2 1 1 1]	15	8
5	1,3	[5 3 2 1 3 1 1 1 1 4 1 2 1 1 2 2]	31	16

For the calculations in this work we chose SiO_2 and TiO_2 as the low and high refractive index materials respectively because these materials are compatible and commonly used to create multilayer structures. The wavelength dependent refractive index of SiO_2 and TiO_2 are given below. The expression for the refractive index for SiO_2 and TiO_2 with λ ranges from 0.2 μm to 4.0 μm is expressed as [23, 94]

$$\mathrm{n_{SiO_2}} = \left(1 + \frac{0.6962\lambda^2}{\lambda^2 - 0.0684^2} + \frac{0.4080\lambda^2}{\lambda^2 - 0.1162^2} + \frac{0.8975\lambda^2}{\lambda^2 - 9.8962^2}\right)^{\frac{1}{2}} \tag{3}$$

and

$$\mathrm{n_{TiO_2}} = \left(5.913 + \frac{0.2441}{\lambda^2 - 0.0803}\right)^{\frac{1}{2}} \tag{4}$$

respectively. In these relations the wavelength is expressed in micrometers.

The loss factor is very low and constant in both SiO_2 and TiO_2 over the entire visible frequency range from 400 nm to 700 nm. In TiO_2 the loss increases rapidly for wavelengths shorter than 350 nm [24]. We accounted for the loss in SiO_2 and TiO_2 by adding an imaginary term to the dielectric constant of 0.0007i for TiO_2 and 0.0001i for SiO_2. These values have been shown to give good agreement between simulation and experimental studies of Bloch surface wave generation in SiO_2 and TiO_2 multilayers [8]. Typical loss values in visible frequency range is in the range of $3e-07$ for SiO_2 and for $5.28333328e-08$ for TiO_2 [24,25].

1.4 MLS Multilayer Structures

The dielectric multilayer reflector is a structure built of alternating layers of high and low refractive index materials with a periodicity assumed here to be along the z-direction. Figure 4(a) shows the general layout of a one-dimensional photonic crystal or Bragg stack, which consists of a dielectric multilayer having high refractive index η_H with length L_H, low refractive index η_L with length L_L, left medium η_a and right medium η_b. The substrate is assumed to be semi-infinite. In contrast to the quarter-wavelength structure, the MLS multilayer is designed using high and low refractive index materials with thicknesses set by an MLS sequence. Figure 4(b) illustrates the 6^{th} order dielectric MLS multilayer structure

designed using the recursive formulation $S_{k+3} = S_{k+1} \oplus S_k$, Where the symbol $\oplus$ represents the binary exclusive or(X-OR) operation. MLS dielectric reflector design has advantages over alternating quarter-wave multilayer (Bragg stack) designs. These structures have flat frequency spectra for desired frequency ranges, and produce broad reflection characteristics for a wide range of angles of incidence.

The optical thickness for the Bragg stack is taken as a quarter wavelength that satisfies $L_H\eta_H{=}\eta_L L_L{=}(\frac{\lambda}{4})$ where λ is the wavelength in vacuum. The incident wave E_{i+}, and reflected wave E_{i-} observed at the left end while transmitted wave E_{i+} at right boundary. The amplitude reflection ($\Gamma = \frac{E_{i-}}{E_{i+}}$) can be calculated using recursive propagation of impedances or reflection responses at interfaces.

$$\rho = \frac{\eta_H - \eta_L}{\eta_H + \eta_L}, \rho_1 = \frac{\eta_a - \eta_H}{\eta_a + \eta_H}, \rho_{M+1} = \frac{\eta_H - \eta_b}{\eta_H + \eta_b} \tag{5}$$

Here, the reflection coefficient is calculated using following parameters: $N = 15$, layers $(2N+1 = 31)$, $\eta_H(TiO_2) = 2.6479$, $\eta_L(SiO_2) = 1.4599$, $\eta_a = 1.0$, $\eta_b = 1.52$ and $\lambda = 550nm$.

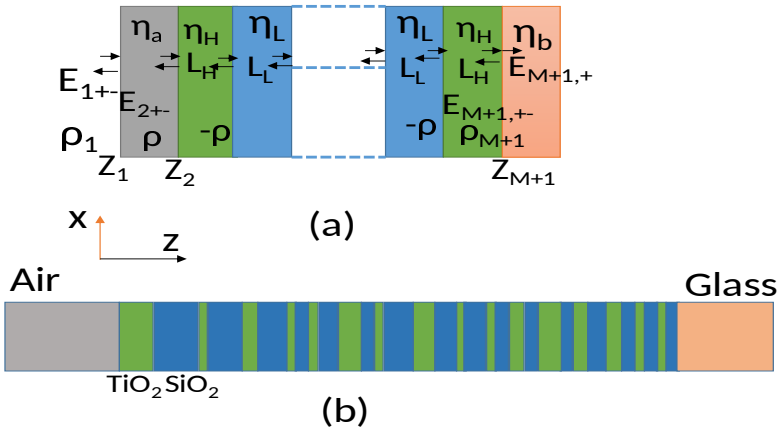

Figure 4: (a) The dielectric alternate high and low refractive index multilayer structure. (b) The 6^{th} order MLS multilayer structure model.

$$Z_2 = \frac{\eta_L^2}{Z_3} = \frac{\eta_L^2}{\eta_H^2} Z_4 = (\frac{\eta_H}{\eta_L})^4 Z_6 .... = (\frac{\eta_H}{\eta_L})^{30} \eta_b \tag{6}$$

Therefore, the generalized impedance is expressed as

$$Z_2 = (\frac{\eta_H}{\eta_L})^{2N}\eta_b \tag{7}$$

The most common multilayer in optical reflection applications is the periodic Bragg reflector built with repeated identical quarter-wave bilayers of low and high refractive index on a substrate (η_a) [26, 27]. Now using $Z_1 = \frac{\eta_H^2}{Z_2}$, the generalized reflection coefficient can be expressed as

$$\Gamma_1 = \frac{Z_L - \eta_a}{Z_L + \eta_a} = \frac{1 - (\frac{\eta_H}{\eta_L})^{2N}\frac{\eta_H^2}{\eta_a\eta_b}}{1 + (\frac{\eta_H}{\eta_L})^{2N}\frac{\eta_H^2}{\eta_a\eta_b}} \tag{8}$$

We obtain amplitude reflectivity $\Gamma_1 = -0.9999$ and $\Gamma_1^2 = 99.98$ as the intensity reflection at the target wavelength. The simplified expression for $\Delta\lambda$ is expressed as:

$$\frac{\Delta\lambda}{\lambda} = \frac{\pi}{2}[\frac{1}{acos(\rho)} - \frac{1}{acos(-\rho)}] \tag{9}$$

With this expression we find $\rho = 0.2894$ and $\Delta\lambda$=213.11 nm for given η_H and η_L. Therefore, this dielectric acts as broadband reflector and is, in principle, capable of reflecting wavelengths ranging from 443.5 nm to 656.6 nm (nearly equal to visible frequency range). The shortcoming of this analytical approach is that the wavelength dependence of the refractive indices of the constituent materials is not taken into account and the calculation is valid only for normal incidence. The calculations in the next section show the reflection of the Bragg stack for wavelength-dependent indices, s- and p-polarization, and for angles away from normal incidence.There is no easy analytical method to derive the reflection for MLS as in the case of the periodic quarter-wave stack and thus, we used a computational approach as described in the following section.

1.5 Bloch Surface Wave Excitation using a Maximum Length Sequence Grating

Diffraction is a general wave phenomena that occurs if a wave front encounters an obstacle, and the portion of wave pass beyond the object interfere to create a diffraction patterns. A diffraction grating is a repetitive array of diffracting elements that produce a periodic alteration of amplitude and phase of the transmitted wave [28]. Diffraction gratings direct light in specific directions as determined by the angle and wavelength of incident light. The diffraction characteristics depends on the period of diffraction grating and the materials used in substrate and superstrate. In the studies here the periodic grating is designed as a corrugation at the surface of alternating quarter-wave high and low index multilayer structures. The corrugation profile of the grating structure is designed using an MLS sequence formulation. Because of the broad range of grating periods, we assume that the MLS diffraction grating is capable of coupling a broad angular range of monochromatic light or a wide spectral range of collimated light into Bloch surface waves on PBG multilayer structures.

When a plane electromagnetic wave is incident on a periodic diffraction grating structure at an angle of θ, the incident wave intensity is diffracted, reflected, or transmitted. The diffraction wavefronts can be found for wavelengths short compared to grating period (Λ). The optical path difference of transmitted diffracted wavefront for positive interference can be expressed in terms of integer multiple of wavelengths [29]. Mathematically,

$$m\lambda = \Lambda(\eta_{II} sin\beta_m - \eta_I sin\theta) \tag{10}$$

where η is refractive index of each medium,$m = ..., -2, -1, 0, +1, +2....$ are the diffraction orders, β_m is transmitted diffracted beam angle, and I and ii represent the first and second layer. For $m = 0$, The angle of refraction, β_0 described by Snell's law as,

$$\beta_0 = \arcsin(\frac{\eta_I}{n_{II}}) sin\theta \tag{11}$$

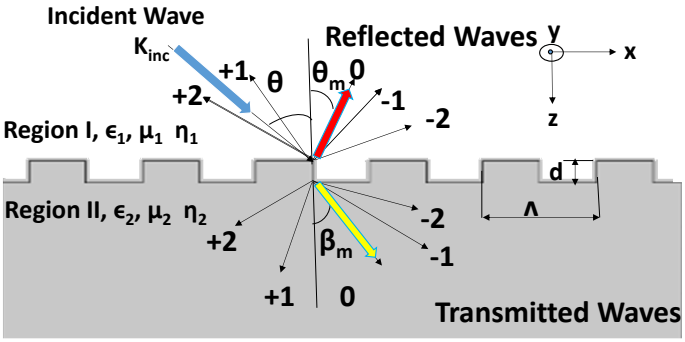

Figure 5: Geometry for periodic rectangular grating showing diffraction for incident plane wave.

The maximum values of sine function varies between -1 and 1, the higher order diffraction order satisfies the condition

$$-(\eta_I + \eta_{II}) < \frac{m\lambda}{\Lambda} < ((\eta_I + \eta_{II}) \tag{12}$$

The extended criteria for non-transmitted diffracted beam of order of 2 or more is

$$\frac{2\lambda}{\Lambda} > (\eta_I \mid sin\theta \mid) + \eta_{II}) \tag{13}$$

The additional defect layer at the top of multilayer structure acts as a suitable active medium for Bloch surface waves [7]. A grating on top of this terminating layer allows light to diffract into BSWs eliminating the need of a bulky prism configuration. The grating profile couples the incident plane wave into the surface mode of photonic crystal when the parallel momentum phase matching criteria is satisfied [18].

This grating can be designed using both periodic or aperiodic structures. Here, we design the grating structure using a maximum length sequence profile. The thickness of grating profile is defined by the MLS sequence. To convert to multilayer thicknesses the A and B correspond to the two different refractive index materials. Thus, the final sequence for N=3 can be expressed as [3 2 1 1] [30, 31]. Figure 6 shows the design of a periodic and a order 3 MLS multilayer design. The periodic structure in figure (a) includes the substrate of 16

alternate multilayer of SiO_2 and TiO_2 along with grating on top of multilayer. Similarly, the MLS grating profile is on top of an identical multilayer. The superstrate material refractive index is varied from 1.32 to 1.34 and the substrate material SiO_2 is wavelength dependent refractive index material.

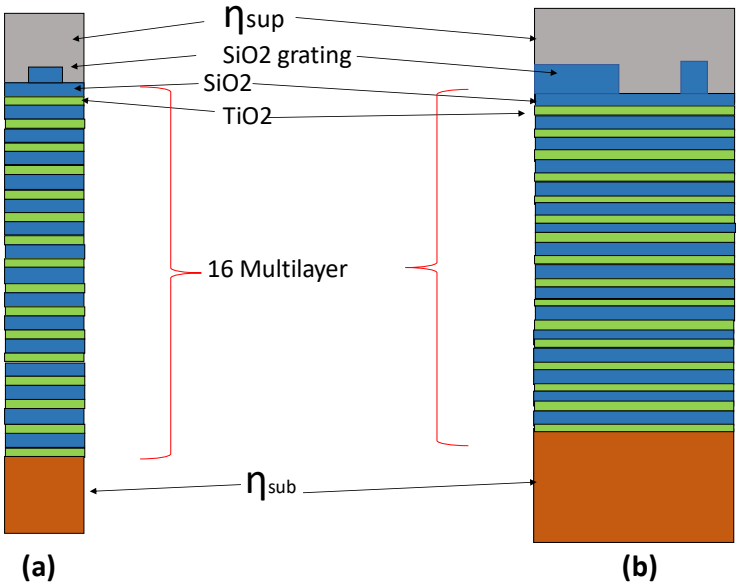

Figure 6: Multilayer design with grating defined by (a) Periodic structure (b) MLS structure at the top of multilayer

1.6 Computational Methods and Tools

There are various computational techniques are used to solve the wave and fields used in electromagnetics (EM). These methods can be classified as numerical, experimental, and analytical. Purely analytical solutions are only available for a small subset of problems. Experimental methods are time consuming and less flexible in terms of parameter variations. However, combined numerical and analytical methods solve EM problems using computationally efficient approximations to Maxwell's equations. The transfer matrix method, finite difference time domain, transmission line modeling method, method of lines, rigorous coupled wave analysis, plane wave expansion method, finite element analysis, and method of moments

are commonly used numerical method to solve electromagnetic problem. The computational study in EM began with development of modern computer technology. Current powerful supercomputers greatly reduce the total computational time for more complex electromagnetic problems. In our research, we are mainly interested in Transfer matrix method (TMM), Rigorous coupled-wave analysis (RCWA) and Finite element method (FEM). FEM is mostly used for solving complex geometries and inhomogeneous media in an efficient way [40]. We used three dimensional COMSOL Multiphysics, which is a cross platform finite element analysis tool, with a user interface which permits easy specification of the system under study and that allows the solution of a coupled system of partial differential equations [41]. The TMM and RCWA methods solve Maxwell's equations for any number of dielectric layers in a semi analytical way. We used our own MATLAB based TMM and RCWA implementations to solve multilayer and grating problems.

CHAPTER 2

COMPUTATIONAL METHODS AND TOOLS

2.1 Computational methods for the response of multilayers

2.1.1 Transfer matrix method

The transfer matrix method (TMM) is a recursive multilayer calculation method using simple matrix operations. The EM fields in each layer in a multilayer structure can be represented as a matrix. The overall response of the multilayer is equivalent to multiplication of each layer matrix. The reflection or transmission through the layer structure is the sum of reflection or transmission through each layers. The reflection through each layer is described by Fresnel equations. [42]

For the formulation of TMM, we start with the set of normalized Maxwell equations describing the field inside a single, isotropic and uniform layer as [37, 39]

$$\nabla \times \mathbf{E} = k_0 \mu_r \tilde{\mathbf{H}} \tag{14}$$

$$\nabla \times \tilde{\mathbf{H}} = k_0 \epsilon_r \mathbf{E} \tag{15}$$

The term k_0 is the free space wave number and is equal to $2\pi/\lambda_0$, where λ_0 is the free space wavelength, $\tilde{\mathbf{H}}$ is equal to $-j\eta_0\mathbf{H}$ is the normalized magnetic field, and η_0 is the free space impedance.

The plane wave solution of these two equation can be written as,

$$\mathbf{E}(\mathbf{r}) = \mathbf{E_0} e^{-j\mathbf{k}.\mathbf{r}} = \mathbf{E_0} e^{-jk_x x} e^{-jk_y y} e^{-jk_z z} \tag{16}$$

$$\mathbf{H}(\mathbf{r}) = \mathbf{H_0} e^{-j\mathbf{k}.\mathbf{r}} = \mathbf{H_0} e^{-jk_x x} e^{-jk_y y} e^{-jk_z z} \tag{17}$$

The repeating boundary condition with tangential component of fields dividing on two media along with phase changes is used to calculate the overall transfer matrix. Fresnel coefficients

are used to find the the reflected and transmitted waves at an interface between two media. These can be expressed as

$$r_{ij}^{s} = \frac{\eta_i cos\theta_i - \eta_j cos\theta_j}{\eta_i cos\theta_i + \eta_j cos\theta_j} \tag{18}$$

$$r_{ij}^{p} = \frac{\eta_j cos\theta_i - \eta_i cos\theta_j}{\eta_j cos\theta_i + \eta_j cos\theta_j} \tag{19}$$

$$t_{ij}^{s} = \frac{2\eta_i cos\theta_i}{\eta_i cos\theta_i + \eta_j cos\theta_j} \tag{20}$$

$$t_{ij}^{p} = \frac{2\eta_i cos\theta_i}{\eta_j cos\theta_i + \eta_j cos\theta_j} \tag{21}$$

where η_i and η_j are the refractive index of i^{th} and j^{th} layer, the superscripts s and p represent s-polarized and p-polarized waves, θ_i and θ_j are the incident and transmitted angle respectively. The sine functions are calculated using Snell's law as $\eta_i sin\theta_i = \eta_j sin\theta_j$. Each time when an electromagnetic wave propagates through the medium, Fresnel's equations are used along with phase change associated with propagation distances [43, 44].

The total reflection r is calculated by summing of waves due to multiple reflection in between first and the last medium. If we are considering three layer with multiple reflection in second layer, the reflection can be expressed as

$$r = r_{12} + t_{12} x t_{21} \tag{22}$$

where x can be expressed as

$$x = e^{i\delta_2} r_{23} e^{i\delta_2}[1 + r_{21}x]; x = \frac{e^{i2\delta_2} r_{23}}{1 - e^{i2\delta_2} r_{23} r_{21}} \tag{23}$$

Similarly, the transmission can be expressed as

$$t = t_{12} y t_{23} \tag{24}$$

where y can be expressed as

$$y = e^{i\delta_2} + yr_{23}e^{i\delta_2}r_{21}e^{i\delta_2}; y = \frac{e^{i2\delta_2}}{1 - e^{i2\delta_2}r_{23}r_{21}} \tag{25}$$

The phase difference at second layer can be expressed as

$$\delta_2 = \frac{2\pi d_2}{\lambda}\eta_2 cos(\theta_2) \tag{26}$$

The total transmission and reflection for TE waver is is calculated by simplifying the above equations

$$t = \frac{t_{i-1,i} * t_{i,i+1}e^{j\delta_i}}{1 + r_{i-1,i} * r_{i,i+1}e^{j2\delta_i}} \tag{27}$$

$$r = \frac{r_{i-1,i} + r_{i,i+1}e^{j2\delta_i}}{1 + r_{i-1,i} * r_{i,i+1}e^{j2\delta_i}} \tag{28}$$

where i represent reflected region (layer) and $(i + 1)$ represents the transmitted layers. In general form these above equation can be represented as

$$\begin{bmatrix} x_i \\ y_i \end{bmatrix} = \tilde{\mathbf{M}}_\mathbf{i} \begin{bmatrix} x_{i+1} \\ y_{i+1} \end{bmatrix} \tag{29}$$

$$\tilde{\mathbf{M}}_\mathbf{i} = \frac{\mathbf{1}}{\mathbf{t_{i-1,i}}} \begin{bmatrix} 1 & r_{i-1,i} \\ r_{i-1,i} & 1 \end{bmatrix} \begin{bmatrix} e^{-j\delta_i} & 0 \\ 0 & e^{-j\delta_i} \end{bmatrix} \tag{30}$$

In this case two neighbouring layer shares the one interfaces. In order to find the field inside the n+1 right layer, we have to multiply from the right with the matrix

$$\frac{1}{t_{n,n+1}} \begin{bmatrix} 1 & r_{n,n+1} \\ r_{n,n+1} & 1 \end{bmatrix} \tag{31}$$

The overall system transfer matrix $\tilde{M}$ is the product of each layer matrix and matrix represented by Equation 28. Mathematically, the system matrix with N layer can be expressed as

$$\tilde{M} = \tilde{M}_1 * \tilde{M}_2 ... \tilde{M}_N * \frac{1}{t_{n,n+1}} \begin{bmatrix} 1 & r_{n,n+1} \\ r_{n,n+1} & 1 \end{bmatrix} \tag{32}$$

2.1.2 Brendel–Bormann Model

Brendel and Bormann (BB) developed a model for a dielectric function by using a Gausian complex error method that reduces an error and provides better results than Lorentz–Drude model functions. Mostly, these dielectric function models are used to find the refractive index and absorption coefficients in certain frequency ranges. We have implemented the BB model to calculate the refractive index of metals (silver and aluminium) in the visible frequency spectrum and compare their reflection characteristics with 7^{th} order maximum length sequence dielectric multilayer structures. By following the mathematical formulation from [57], the complex refractive index for any dielectric or metal can be expressed as

$$\hat{\epsilon_r}(\omega) = \hat{\epsilon}_r^f(\omega) + \hat{\epsilon}_r^b(\omega) \tag{33}$$

where $\hat{\epsilon}_r^f(\omega)$ and $\hat{\epsilon}_r^b(\omega)$ represent the free electron and bound electron effects with oscillator strength f_0 and damping constant Γ_0. The approximate dispersion properties described by Drude model [61] is given by

$$\hat{\epsilon}_r^f(\omega) = 1 - \frac{\Omega_p^2}{\omega(\omega - i\Gamma_0)} \tag{34}$$

where Ω_p is associated with intra band transition and can be expressed as $\Omega_p^2 = \sqrt{\mathcal{F}_0}\omega_p$; ω_p is the plasma frequency. With an additional Lorenzian term described by a semiquantum model, the Lorentz model is given by,

$$\hat{\epsilon}_r^b(\omega) = \sum_{j=1}^{k} \frac{f_j \omega_p^2}{(\omega_j^2 - \omega^2) + i\omega\Gamma_j} \tag{35}$$

where k is the number of oscillators. The Brendel-Borman model uses a Gaussian line shape function which provides a better result than a Lorentzian shape function. The Lorentzian exhibits higher absorption. For the same weight and full-width half-maximum, the Lorentzian wings are usually higher and more extended as compared to a Gaussian. Therefore, the Lorentzian term is replaced by the BB polynomial function,χ_j and that can be expressed

as [57],

$$\hat{\epsilon_r}(\omega) = 1 - \frac{\Omega_p^2}{\omega(\omega - i\Gamma_0)} + \sum_{j=1}^{k} \chi_j(\omega) \tag{36}$$

where $\chi_j(\omega)$ is

$$\chi_j(\omega) = \frac{1}{\sqrt{2\pi\sigma_j}} \int_{-\infty}^{+\infty} exp[-\frac{(x-\omega_j)^2}{2\sigma_j^2}] \times \frac{f_j\omega_p^2}{(x^2-\omega^2) + i\omega\Gamma_j} dx \tag{37}$$

here k is the number of BB oscillators used to interpret the inter-band part of the spectrum. This flexible analytic function provided by BB model has a capability to model a variety of absorption profiles by deriving different wing shape functions. Equation 37 can be solved analytically and the solution of this equation is available in most versions of scientific software like Mathematica, python or C++ etc [58, 59].The real and imaginary parts of the complex refractive index $\hat{N} = \eta - ik$, can be calculated as

$$\eta = \frac{1}{\sqrt{2}}[(\epsilon_{r1}^2 + \epsilon_{r2}^2)^{1/2} + \epsilon_{r1}]^{1/2} \tag{38}$$

$$k = \frac{1}{\sqrt{2}}[(\epsilon_{r1}^2 + \epsilon_{r2}^2)^{1/2} - \epsilon_{r1}]^{1/2} \tag{39}$$

where ϵ_{r1} and ϵ_{r2} relative refractive index of medium 1 and medium 2 respectively.

2.2 Computational methods for the response of gratings

2.2.1 Rigorous coupled wave analysis

The rigorous coupled wave analysis (RCWA) is commonly used method to solve Maxwell equations for periodic diffraction grating structures. It has been used to analyze the transmission and reflection characteristics of different metallic and dielectric wave guide structures [35]. RCWA solves Maxwell's equations for any number of dielectric layers in a semi analytical way in the direction of wave propagation. It uses transformation of the wave equation into eigen vectors of a set of ordinary and partial differential equations. These

eigen vectors can be related to Fourier expansion of permeability(μ_r), permittivity(ϵ_r) and wave propagation characteristics of grating materials [36].

For the formulation of the RCWA semi-analytical method, we start with a set of normalized Maxwell equations describing the field inside the single, isotropic and uniform layer of grating device as [37, 39]

$$\nabla \times \mathbf{E} = k_0 \mu_r \tilde{\mathbf{H}} \tag{40}$$

$$\nabla \times \tilde{\mathbf{H}} = k_0 \epsilon_r \mathbf{E} \tag{41}$$

The term k_0 is the free space wave number and is equal to $2\pi/\lambda_0$, where λ_0 is the free space wavelength, $\tilde{\mathbf{H}}$ is equal to $-j\eta_0\mathbf{H}$ is the normalized magnetic field , and η_0 is the free space impedance. The coupled matrix form can be obtained by expanding these two vector equations 40 and 41 into six different partial differential equation and the eliminating z component from these equations as,

$$\frac{d}{dz'} \begin{bmatrix} \mathbf{s^x}_i(z') \\ \mathbf{s^y}_i(z') \end{bmatrix} = \mathbf{P_i} \begin{bmatrix} \mathbf{u^x}_i(z') \\ \mathbf{u^y}_i(z') \end{bmatrix}, \tag{42}$$

$$\frac{d}{dz'} \begin{bmatrix} \mathbf{u^x}_i(z') \\ \mathbf{u^y}_i(z') \end{bmatrix} = \mathbf{Q_i} \begin{bmatrix} \mathbf{s^x}_i(z') \\ \mathbf{s^y}_i(z') \end{bmatrix}, \tag{43}$$

where $z' = k_0 z$ is a normalizing component.The s_i^x, s_i^y ,u_i^x and u_i^x are the column vectors containing the complex amplitudes of spatial harmonics for electric and magnetic fields respectively. Typically the electric field E_x can be represented as,

$$E_i^x(x,y,z) = \sum_{m=-\infty}^{\infty} \sum_{n=-\infty}^{\infty} s_{i,m,n}^x(z) e^{-j(k_{m,n}^x + k_{m,n}^y)} \tag{44}$$

$$H_i^x(x,y,z) = \sum_{m=-\infty}^{\infty} \sum_{n=-\infty}^{\infty} u_{i,m,n}^x(z) e^{-j(k_{m,n}^x + k_{m,n}^y)} \tag{45}$$

where $\mathbf{K_x}$ and $\mathbf{K_y}$ are diagonal matrices can be represented as,

$$k_{m,n}^x = k_{inc}^x - \frac{2\pi m}{\Lambda_x}, \qquad m = -\infty, ..., -2, -1, 0, 1, 2, ..., \infty \tag{46}$$

$$k^y_{m,n} = k^y_{inc} - \frac{2\pi n}{\Lambda_y}, \qquad n = -\infty, ..., -2, -1, 0, 1, 2, ..., \infty \tag{47}$$

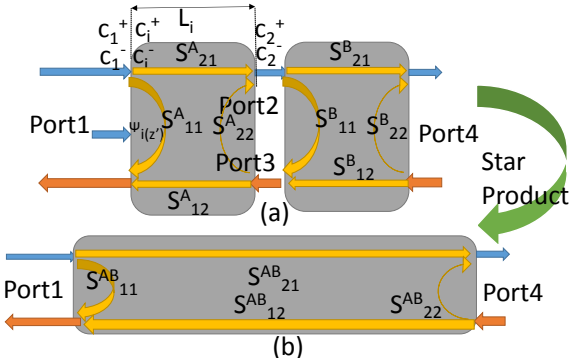

Figure 7: (a) Scattering matrix modeling for two layer grating (b) Redheffer star product.

The quantities P and Q are represented as,

$$\mathbf{P_i} = \begin{bmatrix} \mathbf{K}_x\epsilon^{-1}_{i,z}\mathbf{K}_y & \mu_{i,z} - \mathbf{K}_x\epsilon^{-1}_{i,z}\mathbf{K}_x \\ \mathbf{K}_y\epsilon^{-1}_{i,z}\mathbf{K}_y - \mu_{i,z} & -\mathbf{K}_y\epsilon^{-1}_{i,z}\mathbf{K}_x \end{bmatrix} \tag{48}$$

$$\mathbf{Q_i} = \begin{bmatrix} \mathbf{K}_x\mu^{-1}_{i,z}\mathbf{K}_y & \epsilon_{i,z} - \mathbf{K}_x\mu^{-1}_{i,z}\mathbf{K}_x \\ \mathbf{K}_y\mu^{-1}_{i,z}\mathbf{K}_y - \epsilon_{i,z} & -\mathbf{K}_y\mu^{-1}_{i,z}\mathbf{K}_x \end{bmatrix} \tag{49}$$

Where $\epsilon_{i,z}$ and $\mu_{i,z}$ are Toeplitz convolution matrices in Fourier space.

Again differentiating the equations 42 and 43 with respect to z', we can write the semi analytical equation as,

$$\frac{d^2}{dz'^2}\begin{bmatrix} \mathbf{s^x}_i(z') \\ \mathbf{s^y}_i(z') \end{bmatrix} = \Omega^2 \begin{bmatrix} \mathbf{s^x}_i \\ \mathbf{s^y}_i \end{bmatrix}, \tag{50}$$

where

$$\Omega^2 = \mathbf{PQ} \tag{51}$$

After calculating the eigen vector W and eigen values λ^2 of Ω^2, the general solution of second order differential equation can be simplified further for analytical solution as,

$$\mathbf{V} = \mathbf{QW}\lambda_i^{-1} \tag{52}$$

$$\Psi_i(z') = \begin{bmatrix} \mathbf{s^x}_i(z') \\ \mathbf{s^y}_i(z') \\ \mathbf{u^x}_i(z') \\ \mathbf{u^y}_i(z') \end{bmatrix} = \begin{bmatrix} \mathbf{W_i} & \mathbf{W_i} \\ -\mathbf{V_i} & \mathbf{V_i} \end{bmatrix} \begin{bmatrix} e^{-\lambda_i z'} & \mathbf{0} \\ \mathbf{0} & e^{\lambda_i z'} \end{bmatrix} \begin{bmatrix} \mathbf{c}^+ \\ \mathbf{c}^- \end{bmatrix} \tag{53}$$

where $\mathbf{W}$ and $\mathbf{V}$ are the eigen modes of electric and magnetic fields, $e^{\lambda_i z'}$, $e^{-\lambda_i z'}$, $\mathbf{c}^+$ and $\mathbf{c}^-$ are forward and backward propagation and amplitude coefficient of eigen modes . We can solve equation 53 using the boundary value scattering problem for each layer. The scattering parameters S^i_{11} (reflection coefficient), S^i_{12} (transmission coefficient), S^i_{21} and S^i_{22} are the matrices that define the scattering characteristics between each layer and among eigen modes [37–39]. These matrices can be related as ,

$$\begin{bmatrix} \mathbf{c}_1^- \\ \mathbf{c}_2^+ \end{bmatrix} = \begin{bmatrix} \mathbf{S}_{11}^{(i)} & \mathbf{S}_{12}^{(i)} \\ \mathbf{S}_{21}^{(i)} & \mathbf{S}_{22}^{(i)} \end{bmatrix} \begin{bmatrix} \mathbf{c}_1^+ \\ \mathbf{c}_2^- \end{bmatrix}, \tag{54}$$

The multilayer scattering parameter can be derived by combining multiple scattering matrix using Redheffer star product method [38]. This method allowed to eliminate common mode coefficient and relate all the scattering matrix as star product, $S^{AB} = S^A \otimes S^B$ as

$$\begin{bmatrix} \mathbf{S}_{11}^{(AB)} & \mathbf{S}_{12}^{(AB)} \\ \mathbf{S}_{21}^{(AB)} & \mathbf{S}_{22}^{(AB)} \end{bmatrix} = \begin{bmatrix} \mathbf{S}_{11}^{(A)} & \mathbf{S}_{12}^{(A)} \\ \mathbf{S}_{21}^{(A)} & \mathbf{S}_{22}^{(A)} \end{bmatrix} \otimes \begin{bmatrix} \mathbf{S}_{11}^{(B)} & \mathbf{S}_{12}^{(B)} \\ \mathbf{S}_{21}^{(B)} & \mathbf{S}_{22}^{(B)} \end{bmatrix} \tag{55}$$

After calculating the Redheffer star product for all layers, the global scattering matrix including reflection and transmission scattering matrix is represented as

$$\mathbf{S}^{(global)} = \mathbf{S}^{(Refl)} \otimes \mathbf{S}^{(gratingdevice)} \otimes \mathbf{S}^{(Trans)} \tag{56}$$

Where $\mathbf{S}^{(Refl)}$can be obtained with $L_i = 0, V_1 = V_i = V_{ref}, V_2 = V_0, and W_2 = W_0, W_1 = W_i = W_{ref}$ and $\mathbf{S}^{(Trans)}$ can be obtained with $L_i = 0, V_2 = V_i = V_{Trans}, V_1 = V_0, and W_1 = W_0, W_2 = W_i = W_{Trans}$.

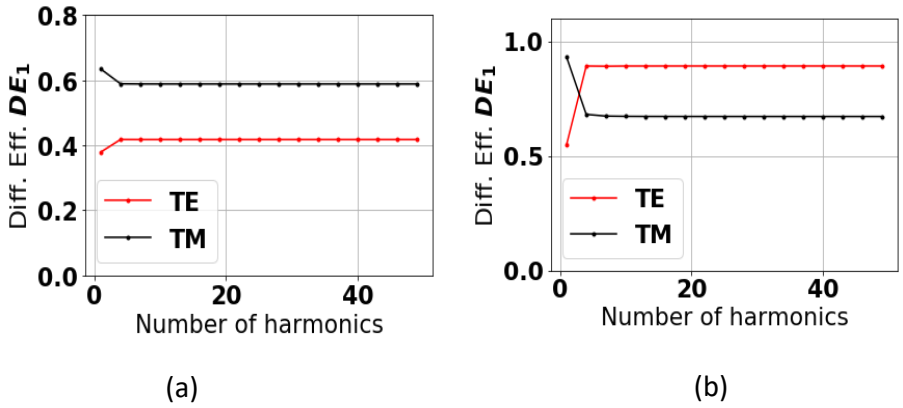

Figure 8: Diffraction efficiency versus normalized groove depth ($\frac{d}{\lambda}$) for (a) $\Lambda = 2\lambda$ and $d = 10\lambda$ (b) $\Lambda = 10\lambda$ and $d = 10\lambda$, with TE and TM polarization ($\theta = 30$ degree, $\eta_1 = 1$ and $\eta_2 = 1.45$

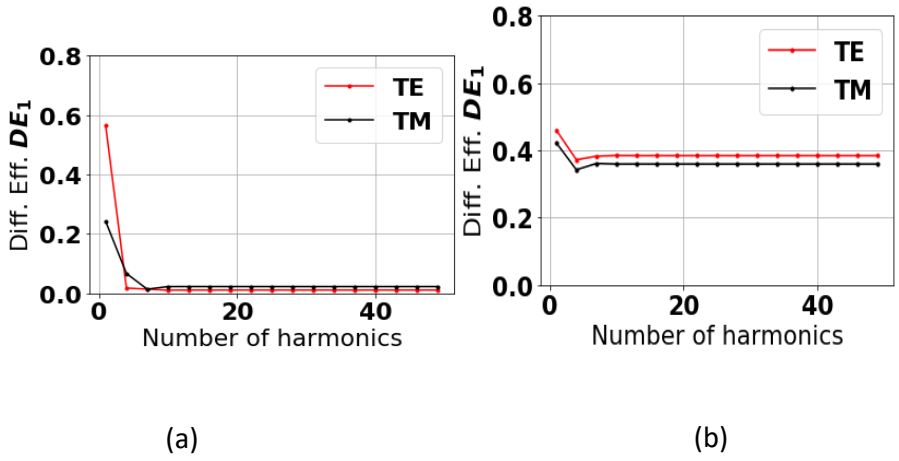

Figure 9: Diffraction efficiency versus normalized groove depth ($\frac{d}{\lambda}$) for (a) $\Lambda = 5\lambda$ and $d = 30\lambda$ (b) $\Lambda = 2\lambda$ and $d = 50\lambda$,with TE and TM polarization ($\theta = 30$ degree, $\eta_1 = 1$ and $\eta_2 = 1.45$

This global scattering matrix relates the input incident wave and transmitted wave as

$$\begin{bmatrix} \mathbf{c}_{Ref} \\ \mathbf{c}_{Trn} \end{bmatrix} = \begin{bmatrix} \mathbf{S}_{11}^{(global)} & \mathbf{S}_{12}^{(global)} \\ \mathbf{S}_{21}^{(global)} & \mathbf{S}_{22}^{(global)} \end{bmatrix} \begin{bmatrix} \mathbf{c}_{inc} \\ \mathbf{0} \end{bmatrix}, \tag{57}$$

where

$$\mathbf{c}_{inc} = \mathbf{W}_{Ref}^{-1} \mathbf{s}_T^{inc} \tag{58}$$

The the $\mathbf{s}_T^{inc}$ related to input incident electric wave that can be related to polarization vector and delta function.

$$\mathbf{s}_T^{inc} = \begin{bmatrix} p_x \delta_{m,n,0} \\ p_y \delta_{m,n,0} \end{bmatrix}, \tag{59}$$

The reflection and transmission coefficient is calculated as

$$\begin{bmatrix} \mathbf{R}_x \\ \mathbf{R}_y \end{bmatrix} = \mathbf{W}_{Refl} \mathbf{c}_{Refl} = \mathbf{W}_{Refl} \mathbf{S}_{11}^{(global)} \mathbf{c}_{inc}$$
$$\mathbf{R}_z = -\mathbf{K}_{z,Refl}^{-1} (\mathbf{K}_x \mathbf{R}_x + \mathbf{K}_y \mathbf{R}_y) \tag{60}$$

$$\begin{bmatrix} \mathbf{T}_x \\ \mathbf{T}_y \end{bmatrix} = \mathbf{W}_{Trn} \mathbf{c}_{Trans} = \mathbf{W}_{Trans} \mathbf{S}_{21}^{(global)} \mathbf{c}_{inc}$$
$$\mathbf{T}_z = -\mathbf{K}_{z,Trans}^{-1} (\mathbf{K}_x \mathbf{T}_x + \mathbf{K}_y \mathbf{T}_y) \tag{61}$$

where

$$\mathbf{K}_{z,Refl} = -\sqrt{\mu_{r,Refl} \epsilon_{r,Refl} \mathbf{I} - \mathbf{K}_x^2 - \mathbf{K}_y^2}$$
$$\mathbf{K}_{z,Trans} = \sqrt{\mu_{r,Trans} \epsilon_{r,Trans} \mathbf{I} - \mathbf{K}_x^2 - \mathbf{K}_y^2} \tag{62}$$

The diffraction efficiencies are related as

$$DE_{Refl} = R_i * R_i * Re(\mathbf{K_{z,Refl}}) / \mathbf{K_{z,inc}}$$
$$DE_{Trans} = T_i * T_i * Re(\mathbf{K_{z,Trans}} \mu_{\mathbf{Refl}}) / (\mathbf{K_{z,inc}} \mu_{\mathbf{Trans}}) \tag{63}$$

The the equation 63 should satisfy for lossless grating design

$$\sum_i DE_{i,Refl} + DE_{i,Trans} = 1 \tag{64}$$

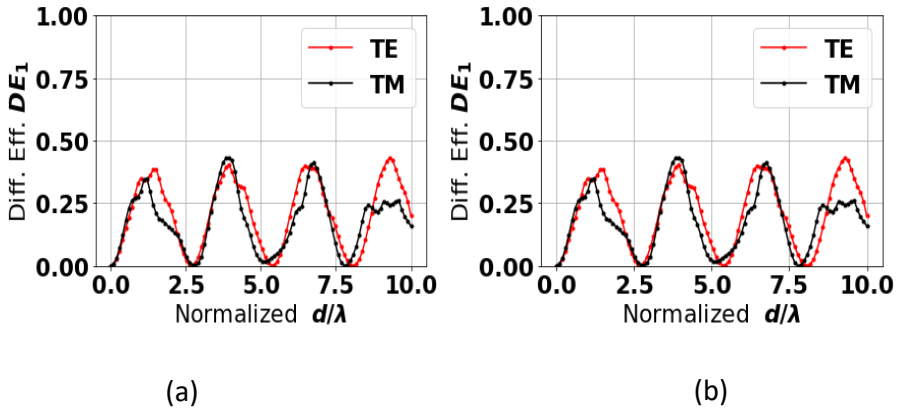

Figure 10: Diffraction efficiency versus Number of harmonics, N for (a) $\Lambda = \lambda$ and $d = \lambda$ (b) $\Lambda = 2\lambda$ and $d = 15\lambda$,with TE and TM polarization ($\theta = 30$ degree, $\eta_1 = 1$ and $\eta_2 = 1.45$

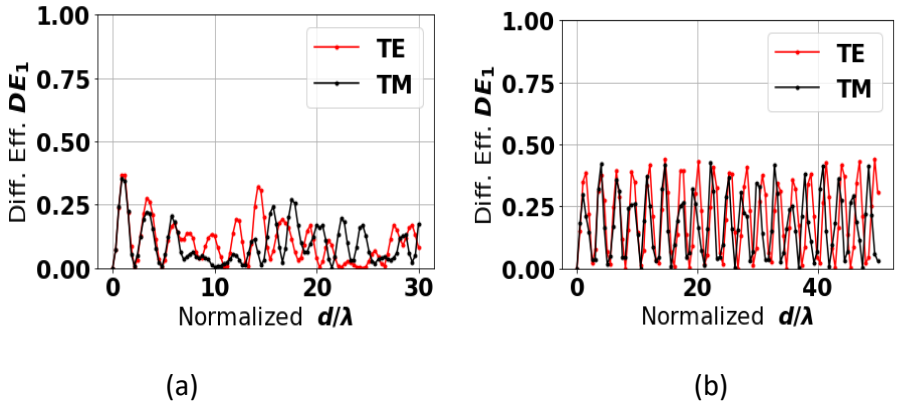

Figure 11: Diffraction efficiency versus Number of harmonics, N for (a) $\Lambda = \lambda$ and $d = \lambda$ (b) $\Lambda = \lambda$ and $d = 50\lambda$, with TE and TM polarization ($\theta = 30$ degree, $\eta_1 = 1$ and $\eta_2 = 1.45$

Figure 8 and Figure 9 show the plot of diffraction efficiency versus normalized depth for a periodic grating structure. This includes the diffraction efficiency for both TE and TM waves incident at an angle of 30 *degree*. The diffraction efficiency is more frequently changed and decreased for higher values of $\frac{D}{\lambda}$ for both TE and TM wave. Similarly, the

Figures 10 and 11 illustrate the plot for efficiency versus number of harmonics with different $\frac{d}{\Lambda}$ and Λ values. The more converged and stable values of diffraction efficiency are found for $d = \lambda$ and $\Lambda = \lambda$. In contrast, the continuously decreasing unstable diffraction efficiency is obtained with higher harmonics for $d = 50 * \lambda$ and $\Lambda = \lambda$.

All these diffraction efficiencies results are obtained by using the Electromagnetics Python (EMpy) tool. The EMpy tool is a python package commonly used to solve isotropic RCWA algorithm and used to produce the frequency response of different structures [35, 45, 46].

2.2.2 Finite-Difference Time-Domain Method

The Finite-Difference Time-Domain method (FDTD) is one of most commonly used full wave techniques to solve electromagnetic problems. This is the simplest time domain technique that can include wide frequency range coverage even for three dimensional problems. This method is widely useful to solve problems such as electromagnetic absorption, radiation, scattering, antennas, radar cross sections, non linear materials etc. The FDTD is a grid based method invented by K.Yee, where time dependent Maxwell equations are discritized both in space and time using central approximations [62–66]. The main idea of the Yee algorithms is to solve the finite difference equations using a leapfrog techniques. First, calculate the **H** field in a given space and at given time then find the **E** field in a given space and at next instant of time and then repeats the process again and again until to reach steady state final condition. Figure 12 and 13 illustrates the 3-D and 2-D Yee lattice structure to solve electromagnetic problems [67]. The 3-D Yee latice is a cubic grid voxel ($\Delta x \times \Delta x \times \Delta x$) where three component of **E** are along the edges and components of **H** are along the faces of cube. Similarly, for 2-D the z component is set zero keeping other x and y component for both **E** and **H** fields. By following the mathematical formulation from [63],the normalized time-dependent Maxwell's curl equations are

$$\nabla \times \mathbf{E} = -\frac{[\mu_{\mathbf{r}}]}{c_0}\frac{\partial \tilde{\mathbf{H}}}{\partial t} \tag{65}$$

$$\nabla \times \tilde{\mathbf{H}} = \frac{[\epsilon_\mathbf{r}]}{c_0}\frac{\partial \mathbf{E}}{\partial t}. \tag{66}$$

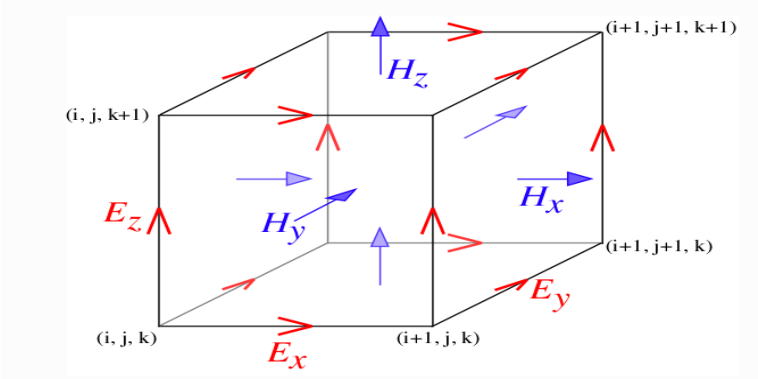

Figure 12: FDTD 3-D Yee Lattice

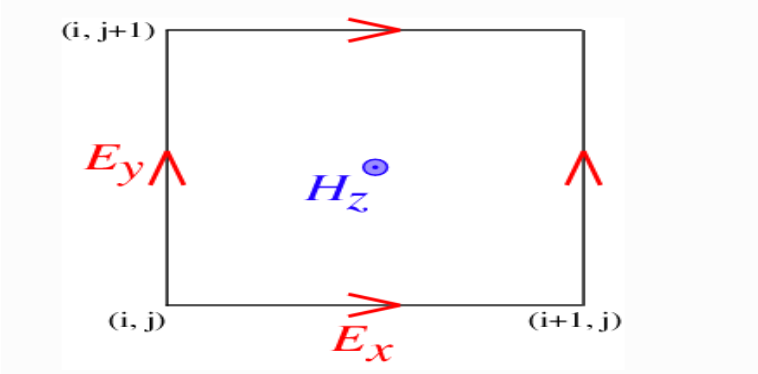

Figure 13: FDTD 2-D Yee Lattice

The final expanded form of Maxwell Equations 65 and 66 can be expressed as

$$\frac{\partial E_z}{\partial y} - \frac{\partial E_y}{\partial z} = -\frac{\mu_{xx}}{c_0}\frac{\partial \tilde{H}_x}{\partial t} \tag{67}$$

$$\frac{\partial E_x}{\partial z} - \frac{\partial E_z}{\partial x} = -\frac{\mu_{yy}}{c_0}\frac{\partial \tilde{H}_y}{\partial t} \tag{68}$$

$$\frac{\partial E_y}{\partial x} - \frac{\partial E_x}{\partial y} = -\frac{\mu_{zz}}{c_0}\frac{\partial \tilde{H}_z}{\partial t} \tag{69}$$

$$\frac{\partial \tilde{H}_z}{\partial y} - \frac{\partial \tilde{H}_y}{\partial z} = \frac{\epsilon_{xx}}{c_0}\frac{\partial E_x}{\partial t} \tag{70}$$

$$\frac{\partial \tilde{H}_x}{\partial z} - \frac{\partial \tilde{H}_z}{\partial x} = \frac{\epsilon_{yy}}{c_0}\frac{\partial E_y}{\partial t} \tag{71}$$

$$\frac{\partial \tilde{H}_y}{\partial x} - \frac{\partial \tilde{H}_x}{\partial y} = \frac{\epsilon_{zz}}{c_0}\frac{\partial E_z}{\partial t} \tag{72}$$

To better understand the theory of the method, we will start by considering simple one-dimensional Maxwell's equations for a wave traveling in the z direction as

$$\frac{\partial E_x}{\partial t} = -\frac{1}{\epsilon_0}\frac{\partial H_y}{\partial z} \tag{73}$$

$$\frac{\partial H_y}{\partial t} = -\frac{1}{\mu_0}\frac{\partial E_x}{\partial z} \tag{74}$$

By considering E_x and H_y shifted in space by half a cell and in time by half a time step and using Taflove normalization of the E field $\tilde{E} = \sqrt{\frac{\epsilon_0}{\mu_0}}E$ and some simplication, the above Equations 73 and 74 can be written as

$$E_x^{n+1/2}(k) = E_x^{n-1/2}(k) - \frac{1}{\sqrt{\epsilon_0\mu_0}}\frac{\Delta t}{\Delta z}(H_y^n(k-1/2) - H_y^n(k+1/2)) \tag{75}$$

$$H_y^{n+1}(k+1/2) = H_y^n(k+1/2) - \frac{1}{\sqrt{\epsilon_0\mu_0}}\frac{\Delta t}{\Delta z}(E_x^{n+1/2}(k) - E_x^{n+1/2}(k+1)) \tag{76}$$

The parameter step size Δz can be chosen that at least 10 cells per wavelength and the time step is also chosen according to stability considerations for the wave propagation. The stability criteria analyzed in by Courant, Friedrichs and Levy and Von Neumann, also called CFL (for Current, Friedrich and Levy), can be expressed [69, 70] as

$$\Delta t \leq \left[v_{max} \cdot \sqrt{\frac{1}{\Delta x^2} + \frac{1}{\Delta y^2} + \frac{1}{\Delta z^2}}\right]^{-1} \tag{77}$$

where v_{max} is the maximum velocity of light propagation. In case of a uniform mesh $\Delta x = \Delta y = \Delta z$, the CFL criterion becomes for 3D

$$\Delta t \leq \frac{1}{v_{max}}\sqrt{\frac{\Delta}{3}} \tag{78}$$

. The final step to implementing any FDTD algorithm is figuring out how to handle the boundaries. The simplest boundary condition (BC) are called the Dirichlet boundary and Neumann boundary conditions, and works by fixing the end points of a simulation to some specified value [68]. Similarly, for 3-D FDTD, the finite difference approximations for 3-D FDTD are as follows

$$\frac{E_z^{i,j+1,k}|_t - E_z^{i,j,k}|_t}{\Delta y} - \frac{E_y^{i,j,k+1}|_t - E_y^{i,j,k}|_t}{\Delta z} = -\frac{\mu_{xx}^{i,j,k}}{c_0}\frac{\tilde{H}_x^{i,j,k}|_{t+\frac{\Delta t}{2}} - \tilde{H}_x^{i,j,k}|_{t-\frac{\Delta t}{2}}}{\Delta t} \tag{79}$$

$$\frac{E_x^{i,j,k+1}|_t - E_x^{i,j,k}|_t}{\Delta z} - \frac{E_z^{i+1,j,k}|_t - E_z^{i,j,k}|_t}{\Delta x} = -\frac{\mu_{yy}^{i,j,k}}{c_0}\frac{\tilde{H}_y^{i,j,k}|_{t+\frac{\Delta t}{2}} - \tilde{H}_y^{i,j,k}|_{t-\frac{\Delta t}{2}}}{\Delta t} \tag{80}$$

$$\frac{E_y^{i+1,j,k}|_t - E_y^{i,j,k}|_t}{\Delta x} - \frac{E_x^{i,j+1,k}|_t - E_x^{i,j,k}|_t}{\Delta y} = -\frac{\mu_{zz}^{i,j,k}}{c_0}\frac{\tilde{H}_z^{i,j,k}|_{t+\frac{\Delta t}{2}} - \tilde{H}_z^{i,j,k}|_{t-\frac{\Delta t}{2}}}{\Delta t} \tag{81}$$

$$\frac{\tilde{H}_z^{i,j,k}|_{t+\frac{\Delta t}{2}} - \tilde{H}_z^{i,j-1,k}|_{t+\frac{\Delta t}{2}}}{\Delta y} - \frac{\tilde{H}_y^{i,j,k}|_{t+\frac{\Delta t}{2}} - \tilde{H}_y^{i,j,k-1}|_{t+\frac{\Delta t}{2}}}{\Delta z} = \frac{\epsilon_{xx}^{i,j,k}}{c_0}\frac{E_x^{i,j,k}|_{t+\Delta t} - E_x^{i,j,k}|_t}{\Delta t} \tag{82}$$

$$\frac{\tilde{H}_x^{i,j,k}|_{t+\frac{\Delta t}{2}} - \tilde{H}_x^{i,j,k-1}|_{t+\frac{\Delta t}{2}}}{\Delta y} - \frac{\tilde{H}_z^{i,j,k}|_{t+\frac{\Delta t}{2}} - \tilde{H}_z^{i-1,j,k}|_{t+\frac{\Delta t}{2}}}{\Delta z} = \frac{\epsilon_{yy}^{i,j,k}}{c_0}\frac{E_y^{i,j,k}|_{t+\Delta t} - E_y^{i,j,k}|_t}{\Delta t} \tag{83}$$

$$\frac{\tilde{H}_y^{i,j,k}|_{t+\frac{\Delta t}{2}} - \tilde{H}_y^{i-1,j,k}|_{t+\frac{\Delta t}{2}}}{\Delta x} - \frac{\tilde{H}_x^{i,j,k}|_{t+\frac{\Delta t}{2}} - \tilde{H}_x^{i,j-1,k}|_{t+\frac{\Delta t}{2}}}{\Delta y} = \frac{\epsilon_{zz}^{i,j,k}}{c_0}\frac{E_z^{i,j,k}|_{t+\Delta t} - E_z^{i,j,k}|_t}{\Delta t}. \tag{84}$$

Meep (an acronym for MIT Electromagnetic Equation Propagation) is a open source package, that implements the finite-difference time-domain (FDTD) method for computational electromagnetics. Meep automatically solves the Yee grid implementations with visualization routines for the simulation domain involving geometries, fields, and boundary layers [71]. It is free and open-source software which has the capability of calculating fields for Poynting flux, near-to-far transformation, local density of states, scattering cross section, and Maxwell stress tensor. Moreover, it uses complete scriptability via any scientific programming and supports distributed-distributed parallel computing along with mirror plane symmetry. In addition, it supports the perfectly-matched layer along with absorbing boundaries that includes an adjoint solver for sensitivity analysis. It has a subpixel smoothing feature for improving accuracy with field import/export in the HDF5 data format [67, 71]. Meep simulations are Python or linux scripts which involve specifying the device geometry,

materials, current sources, monitor fields, and other parameter sweeps and optimizations. Especially, python scripts provides more flexibility on simulation that includes most of the python libraries like Matplotlib, Scipy and Numpy. In order to execute Meep simulation we just need to use the linux command *pythontestsimulation.py > output.out*. This command reads the Python script *testsimulation.py* and execute it and produces output and saves the output to the file. *output.out* [67, 71].

2.2.3 Finite Element Method

The Finite Element Method (FEM) is the most commonly used tool to model complex structures where the problems are expressed in terms of partial differential equations (PDEs). It provides a very stable and good discretized approach to approximate the PDEs even for curved surfaces using different numerical techniques. This method is based on the weak formulation of the Galerkin method associated for a partial differential equation (PDE) boundary value problem (BVP). The Galerkin method uses the multiplication of a calculated residual from the PDE with a weight function and integrates over single elements. In addition, the weight functions are selected from the same set of functions as the interpolation function in order to solve a second order partial differential equation. Therefore this technique is also called weighted-residual weak formulation. The main steps to solve FEM using Galerkin method include: discretize or subdivision of the domain, selection of proper interpolation functions, weak formulation of the system of equations using boundary conditions, form the global matrix system of equations, impose Dirichlet boundary conditions, solve the linear system of equations, and post process the results [50, 51]. Comsol Multiphysics is one of the mostly widely used FEM tools to solve engineering and mathematical problems within a modeling domain. In the RF module of Comsol Multiphysics the four major steps to solve any finite element problem include: Model set-up, meshing, solving, and post processing. The model set-up usually involves model creation, boundary setup, and defining the governing equations. Similarly, the meshing and solving includes the domain

discritization and solving a set of linear equation described by fields respectively. Finally, post processing includes the extraction and interpretation of meaningful information from the simulated fields. [52].

By following [53] the mathematical details of the time-harmonic Maxwell equation factorization for the finite element method, the equation for the E field with conductivity σ, permittivity $\hat{\epsilon} = \epsilon - j\sigma/\omega$ can be expressed as:

$$\nabla \times \left(\frac{1}{j\omega\mu}\nabla \times \mathbf{E}\right) + j\omega\hat{\epsilon}\mathbf{E} = \mathbf{0} \tag{85}$$

Because the finite element method is based on the weak formulation, the Equation 85 can be expressed in term of scalar basis functions ϕ_i and an unknown vector field E_i as

$$E = \sum_i E_i \phi_i \tag{86}$$

Galkerin's approximation using the weak formulation over the integration of interest around the boundary of $\langle \quad \rangle$ and edge element expansion with basis function N_i can be expressed as

$$\left\langle \left(\frac{1}{j\omega\mu}\nabla \times \mathbf{E}\right) \bullet (\nabla \times N_i) \right\rangle + \langle j\omega\hat{\epsilon}\mathbf{E} \bullet \mathbf{N_i} \rangle = -\oint \frac{\mathbf{1}}{\mathbf{j}\omega\mu}\hat{\mathbf{n}} \times (\nabla \times \mathbf{E}) \bullet \mathbf{N_i}\mathbf{ds} \tag{87}$$

The important concepts of the Galkerin's weak approximation are to satisfy the Helmhotz equation and the conservation of energy in the electromagnetic field over the integration domain. If we replace N_i with E^* and using Faraday's law of relations $B = \mu H$, the Equation 87 satisfies the time harmonics Farady's law and Poynting's theorem of $\langle -j\omega\mathbf{B} \bullet \mathbf{H}^* \rangle + \langle j\omega D^* \bullet \mathbf{E}^* \rangle = \oint (\mathbf{E} \times \mathbf{H}*) \bullet \hat{\mathbf{n}}\mathbf{ds}$.

For each basis function of N_j in Equation 87, the numerical approximation for M degrees of freedom can be expressed in terms of linear system of equation with stiffness matrix, A_{ij} and forcing vector f_{ij} as,

$$E = \sum_{i=1}^{M} A_{ij} E_i = f_j \tag{88}$$

$$A_{ij} = \left\langle \left(\frac{1}{j\omega\mu} \nabla \times N_i \right) \bullet (\nabla \times N_j) \right\rangle + \langle j\omega\hat{\epsilon}\mathbb{N}_i \bullet N_j \rangle \tag{89}$$

$$f_j = -\oint \frac{1}{j\omega\mu} \hat{n} \times (\nabla \times \mathbf{E}) \bullet N_j ds \tag{90}$$

Here, the edge element satisfies the continuity and uniqueness theorems for tangential components of both electric and magnetic fields across all the boundaries. One of the most popular versions of the edge element is Whitney 1-form with tetrahedral mesh which includes the wedges and corner with Drichlets boundary conditions [54]. In tetrahedron mesh of Whitney-1 form, the circulation of $N_e = W_e$ is 1 and 0 along edge e and other edges respectively.The unknown E_i can be related as $E = \sum_i^6 E_e W_e$. Very accurate and higher resolution approximations are not possible with this first order Whitney approximation. Therefore, several other researchers have been working on higher order and hybrid approximation to improve the interpolation error with more computational complexity and accurate convergence [55, 56].

2.3 Summary

This chapter includes the mathematical details of different computational electromagnetic methods to solve the fields and waves. We include the Transfer matrix method (TMM), Brendel- Bormann (BB) model, Rigorous coupled-wave analysis (RCWA), Finite-Difference Time-Domain method (FDTD) and Finite element method (FEM). We mostly employed the TMM and BB model for MLS multilayer project and RCWA,FDTD, FEM for grating projects. COMSOL Multiphysics, which is a cross platform finite element analysis tool, with a user interface which permits easy specification of the system.

CHAPTER 3

MAXIMUM LENGTH SEQUENCE DIELECTRIC MULTILAYER REFLECTOR

3.1 Introduction

This computational investigation examines the response of optical multilayers consisting of alternating high and low refractive index materials with a thickness profile determined by a pseudo-random maximum length sequence (MLS). The aim is to demonstrate that such multilayers have higher reflectivity over a broader bandwidth than periodic multilayers with the same index contrast and number of layers. For periodic multilayers, the forbidden transmission bandwidth, the photonic band gap of the one dimensional photonic crystal, is set by the index contrast between the two materials. Higher index contrast leads to band gaps with broader frequency coverage [7, 8]. A maximum length sequence (MLS) is a two-level pseudo-random binary sequence which has a uniformly flat frequency response except for a DC offset [1]. The flat frequency response indicates that these sequences contain equal amplitudes of all possible periodicities [2–4]. We posit that a multilayer using a thickness profile determined by an MLS will have a broader range of periods and, hence, will exhibit a wider bandgap than a periodic system of the same materials and number of layers.

The aim of this study is twofold. First, we explore the feasibility of creating a functional omnidirectional reflector across all wavelengths in the visible without the necessity of materials with extremely high index contrast. Periodic dielectric multilayers act as near perfect reflectors over a limited wavelength and angular range and provide excellent reflectivity, low absorption loss, and a high degree of robustness compared to metallic reflectors [72]. However, periodic dielectric multilayer reflectors are not highly reflective of light coming from any direction and polarization. In general, the range of reflected wavelengths shifts to the blue at angles away from normal incidence. An ideal omnidirectional dielectric multilayer

reflector would have near perfect reflection for all wavelengths in a given range and at all incident angles and any polarization. In the visible range, metallic mirrors from materials such as silver and aluminum have such properties [73, 74]. The goal here is to make a metallic-like reflector from a multilayer structure using the deterministically pseudo-random maximum length sequence thickness profile. The second longer-term objective is to begin the exploration of photonic band gaps in aperiodic structures in two and three dimensions. In this work, the wavelength and angular reflection from pseudo-random MLS multilayers are compared with that for metallic mirrors and for purely periodic systems based on quarter-wavelength multilayers. Future work will explore the prospect of two- and three- dimensional structures with MLS index profiles.

Aperiodic multilayer structures with thickness profiles defined by Thue-Morse, Fibonacci, and Rudin-Shapiro algorithms have been studied before, of particular interest in these quasi-periodic systems is the phenomenon of localization [79–87, 97–101].

However, to our knowledge the maximum length sequence profile multilayer has only been studied for its electromagnetic wave properties in its ability to support Bloch surface waves [79]. In acoustics there is a long history of using the perfectly random profile of an MLS defined grating to create diffusers that diffract sound equally in all directions [75].

Other methods to enhance the reflectivity of multilayers on one dimensional reflectors using random disorder and inhomogeneity have been explored [76, 77, 102]. These designs use alternate high and low refractive index layer structures with random variations of layer thicknesses. The results are thus dependent on the choice of randomization algorithm or on some optimization routine. In contrast, the MLS offers a deterministic layer thickness profile with flat Fourier response; the MLS sequence is often described as being ideally random.

3.2 Simulation Results and Discussions

We conducted our numerical simulations both using the transfer matrix method (TMM) and verified the results independently using a recursive calculational model, both commonly used

techniques to analyze the electromagnetic propagation through multilayer films. TMM is based on the boundary condition of Maxwell's equations where the electric field at the end of the layer can be derived using matrix operations for a given field at the beginning of a layer. The reflection from a multilayer structure is the transformation of the overall system matrix, which is the product of each layered matrix. Here, we implemented the simulations using Matlab R 2017 and Python 3.6.

Simulations were performed for both N=6 and N=7 MLS multilayer structures. For N=6 the number of layers is 34 with a total multilayer thickness of 5.06 μm. For N=7 the number of layers is 66 with a total multilayer thickness of 9.63 μm. Current fabrication methods allow multilayers of up to 600 layers and a total thickness of 23 μm [78]. Figure 14 illustrates the reflection characteristics for the 6^{th} order MLS multilayer for both s- and p-polarized light incident with 0°, 30°, and 60° respectively.

As indicated from Table 1, This multilayer contains 32 layers consisting of alternating SiO_2 and TiO_2 layers with thicknesses scaled by the MLS sequence. In this case, the smallest layer thickness is 519 nm for TiO_2 and 941 nm for SiO_2. Clearly, the reflection curves contain significant structure with many reflectivity dips as a function of wavelength. However, exclusive of the narrow dips, there is high reflectivity at all incident angles across all the wavelengths in the visible (400 nm to 700 nm).

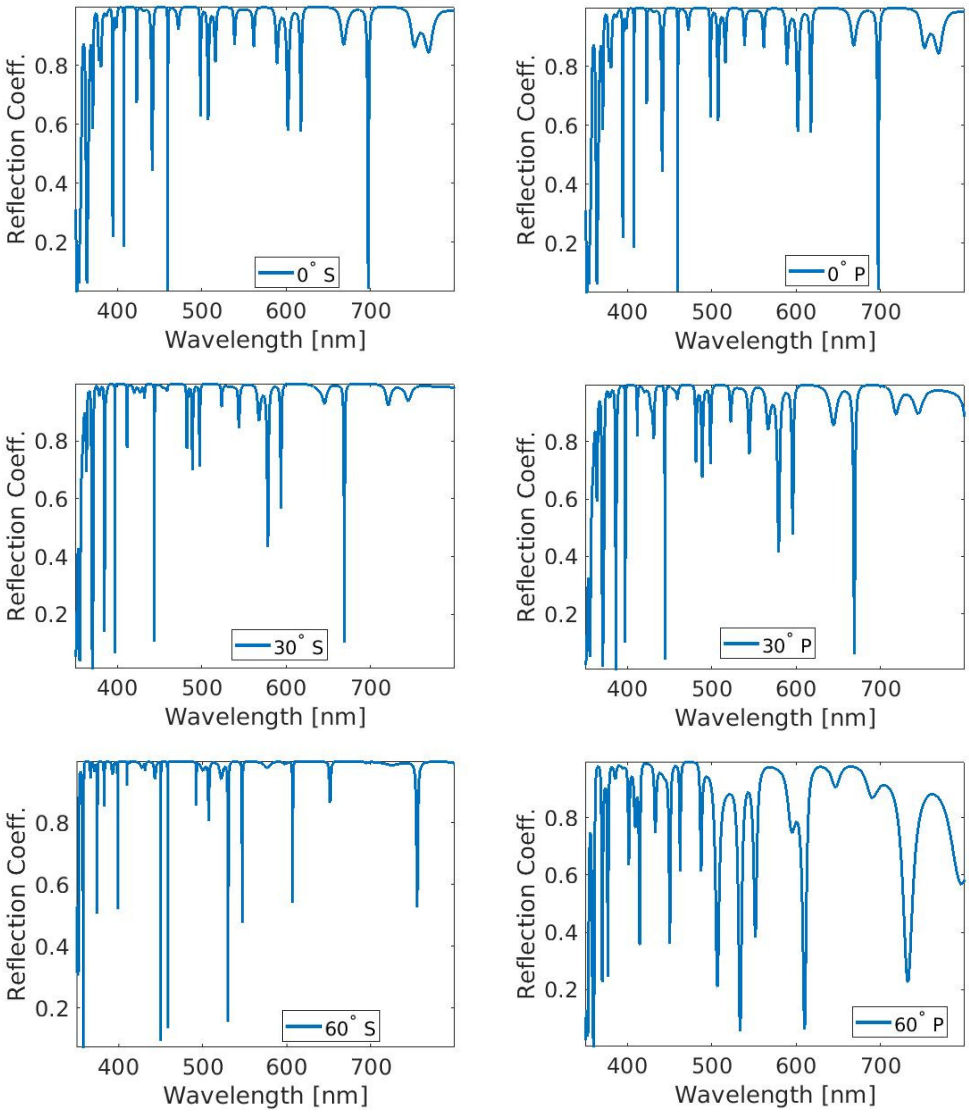

(a) S polarized wave

(b) P polarized wave

Figure 14: Reflection characteristics for 6^{th} order MLS multilayer structure for both s- and p-polarized light incident with 0°, 30°, and 60° respectively.

Many of the dips in reflectivity are very narrow, on the order of 2 nm or less, and thus have little effect on the overall reflectivity across all visible wavelengths. To assess the effectiveness of the multilayer as an omni-directional reflector, the metric we chose to compare the reflectivity of the MLS systems with periodic multilayers and with metallic

reflectors is the average reflectivity taken over the wavelength range from 400 nm to 700 nm. For s-polarized light, the average reflection in visible frequency range of 400 nm to 700 nm is more than 95 percent at all incident angles. For p-polarized light, the average reflectivity is lower, particularly in the vicinity of Brewster's angle, as expected, at around 60°. The specific average reflection values are summarized in Table 2 order MLS . The first point of comparison for the MLS reflectivity for N=6 is to contrast the results with the reflectivity of a periodic multilayer with the same number of layers and index transitions. Figure 15 illustrates the characteristics for 32 layer alternate high and low index multilayer structure for both s- and p-polarized light incident at 0°, 30°, and 60° respectively.

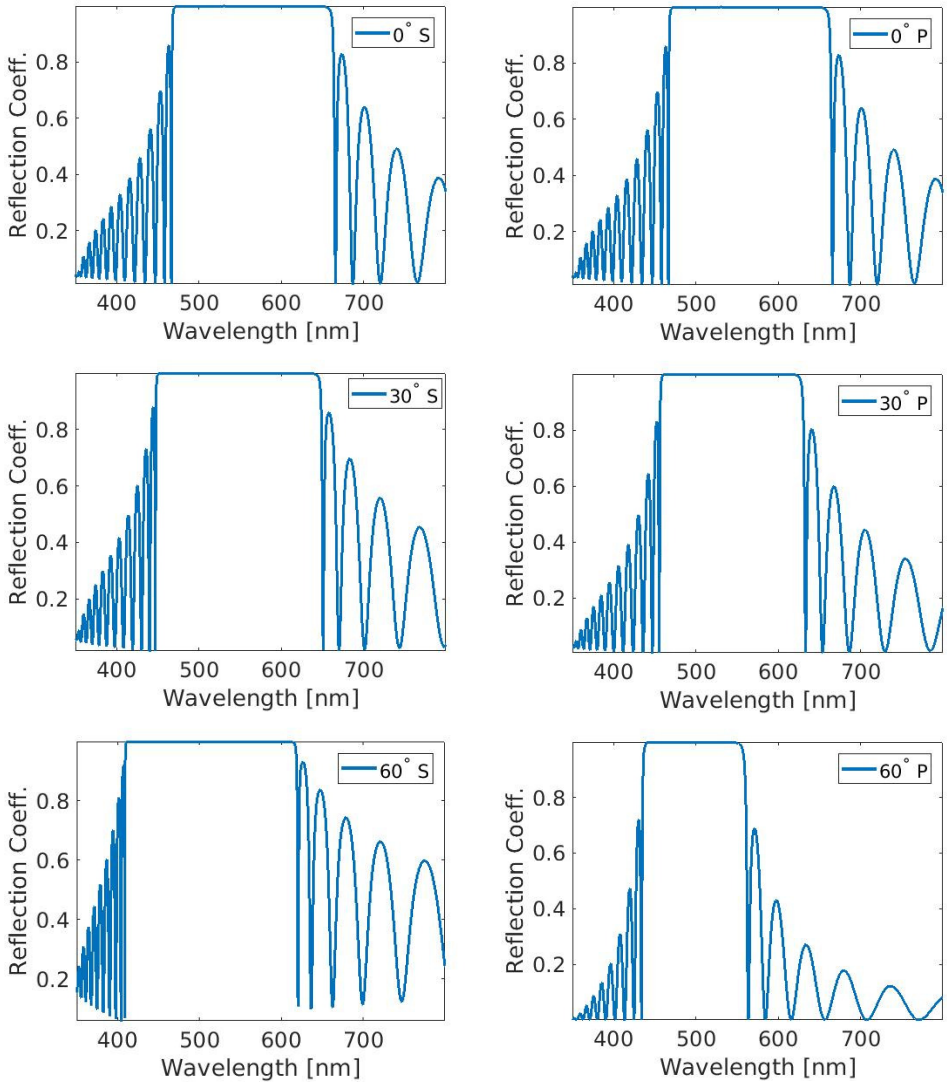

(a) S polarized light

(b) P polarized light

Figure 15: Reflection characteristics for 32 layer alternate high and low index multilayer structure for both s- and p-polarized light incident with 0°, 30°, and 60° respectively.

These graphs indicate that the periodic multilayers are essentially perfect reflectors for a narrow range centered about the design wavelength of 550 nm. However, the high reflectivity does not encompass the entire visible range and falls off in such a way that the average reflectivity across the entire visible range is notably lower compared to 6^{th} order

MLS multilayer structure. Table 3 summarizes the average reflection for the periodic multilayer structure. As the table indicates, the average reflectivity for the MLS multilayer is between 10% and 15% higher than the periodic multilayer for s-polarized light and between 15% and 30% higher than the periodic multilayer for p-polarized light. Figure 16 plots the average reflection in the visible frequency range as a function of incident angle for the 6^{th} order ($N = 6$) MLS and the 32 layer alternate high and low index multilayer structure for both s- and p-polarized light. This plot verifies the omni-directional reflection characteristic of the MLS multilayer. For s-polarized light in the visible range, the reflection at all angles is greater than 95%. The p-polarized light has lower reflectivity at larger angles compared to s-polarized light for both MLS and alternate high and low index multilayer, but it is still above 80%.To answer the question of whether the MLS system should be improved, we next calculated the MLS reflectivity for the N=7 MLS sequence.

Table 2: Average reflection coefficient for different 6^{th} order MLS for both s- and p-polarized light.

Incident angle(deg)	s-polarized light	p-polarized light
0	0.9561	0.9561
30	0.9721	0.9465
60	0.9867	0.8638

Table 3: Average reflection coefficient for 32 layer alternate high and low index multilayer for both s- and p-polarized light

Incident angle(deg)	s-polarized light	p-polarized light
0	0.7909	0.7909
30	0.8231	0.7292
60	0.8795	0.5432

Figure 17 shows the reflection characteristics for 7^{th} order MLS multilayer structure for both s- and p-polarized light incident with 0°, 30°, and 60° respectively. The 7^{th} order MLS

multilayer structure thickness is determined by following an alternate high and low refractive index sequence: [7, 4, 3, 1, 4, 2, 1, 1, 2, 2, 1, 2, 1, 6, 1, 3, 1, 2, 2, 3, 1, 1, 3, 1, 1, 1, 2, 1, 2, 5, 2, 2, 2, 1, 1, 1, 1, 2, 3, 2, 4, 1, 2, 1, 1, 4, 6, 5, 1, 1, 2, 1, 1, 1, 3, 2, 1, 3, 3]. This sequence length is 127 (=2^7-1) which converts to 64 distinct high and low index layers.

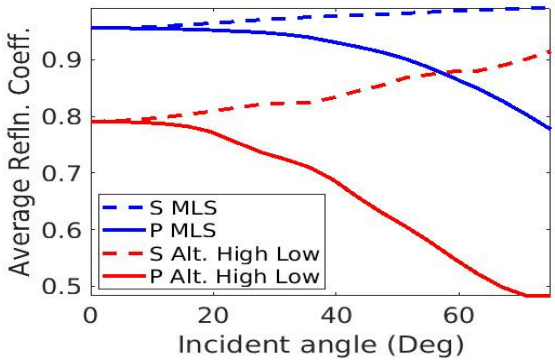

Figure 16: Average reflection as function of incident angle in the visible frequency range for 6^{th} order ($N = 6$) MLS and 32 layer alternate high and low index multilayer structure for both s- and p-polarized light.

Simulations for the 7^{th} order MLS again show significant structure with many very narrow dips in the reflection curve. However, the average reflection in visible frequency range of 400 nm to 700 nm is more than 96% for s-polarized light at all angles.The reflectivity at 60° and 30° respectively is 98.39% and 96.29% for s-polarized light and 91.83% and 95.58% for p-polarized light. Table 4 summarizes the average reflection for 7^{th} order MLS multilayer structure for both s- and p-polarized light. The N=6 and N=7 MLS multilayers would function better in practice than the plots imply if the incident light being reflected had even a small angular spread in which case the effect of the narrow dips at specific angles would be blurred because of the angular shift of the narrow minima.For a better point of reference of the MLS system as an omni-directional reflector, we compare the average reflection results with those for two metals, silver and aluminum, with high reflectivity throughout the visible.

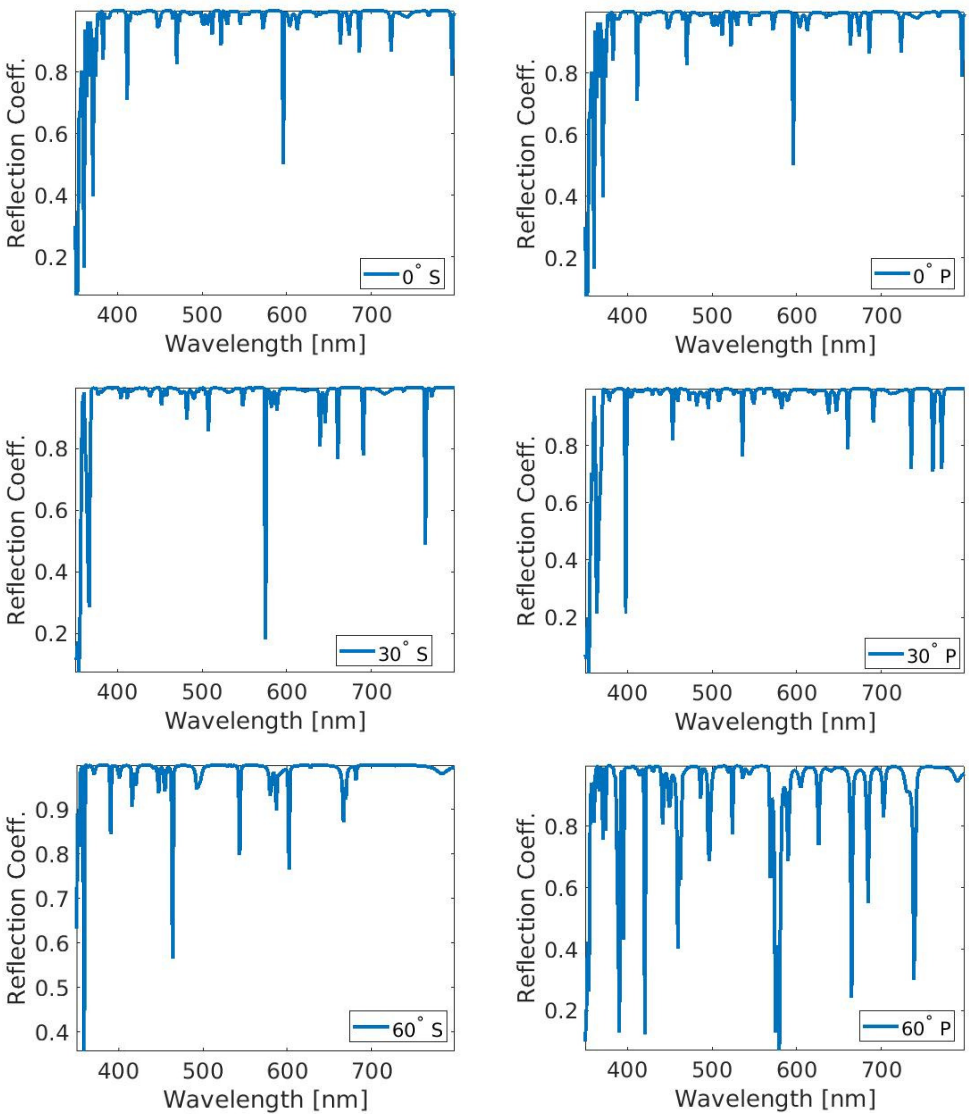

(a) S polarized light

(b) P polarized light

Figure 17: Reflection characteristics for 7^{th} order MLS multilayer structure for both s- and p- polarized light incident with 0°, 30°, and 60° respectively.

The wavelength-dependent refractive index of the two metals in the visible frequency range is determined using a Brendel- Bormann (BB) model. The BB model provides the most accurate real and imaginary permittivity values for the materials by using a Gaussian complex error function [74]. For the aluminum metallic reflector, we calculated s-polarized

reflectivities of 95.76% and 92.73% and p-polarized reflectivities of 84.66% and 96.74% for light incident at 60° and 30° respectively. Similarly, for silver, we found 98.12% and 95.64% reflectivity for s-polarized light and 93.22% and 95.64% for p-polarized light incident at 60° and 30° respectively. Further, 91.63% and 96.22% reflection is achieved for light at normal incidence respectively for aluminum and silver metallic reflectors. Table 5 summarizes the average reflection for metallic reflectors for both s- and p-polarized light. Figure 18 plots the reflection characteristics as a function of wavelength for metallic reflectors in the visible frequency range for incident angles of 0°, 30°, and 60°.

Figure 19 plots the average reflectivity for the N=7 MLS multilayer for the two metals for both s- and p-polarized waves. The plots demonstrate that the average reflection for the 7^{th} order MLS is higher than that of both metallic reflectors. Clearly, the MLS has slightly higher reflectivity than the silver and much better reflectivity than aluminum for s-polarized wave. The graphical illustration in Figure 19 indicates that the MLS reflector is effectively achieving omni-directional reflection for all angles in the visible wavelength range of 400 to 700 nm.

Table 4: Average reflection coefficient for different 7^{th} order MLS for both s- and p-polarized light.

Incident angle(deg)	s-polarized light	p-polarized light
0	0.9637	0.9637
30	0.9629	0.9558
60	0.9839	0.9183

Table 5: Average reflection coefficient for metallic reflectors for both s- and p-polarized light.

Incident angle(deg)	Al(s-pol.)	Al(p-pol.)	Ag(s-pol.)	Ag(p-pol.)
0	0.9163	0.9163	0.9622	0.9622
30	0.9273	0.9039	0.9674	0.9564
60	0.9576	0.8466	0.9812	0.9322

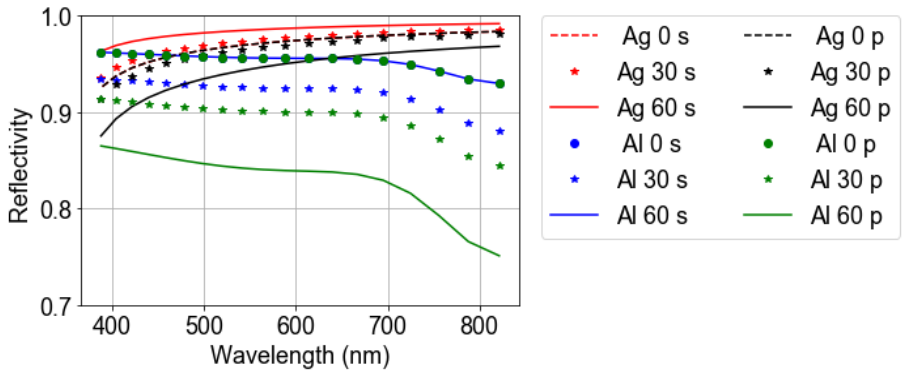

Figure 18: Reflection characteristics for metallic reflectors in visible frequency range for both s- and p-polarized light incident at an angle of 0°, 30°, and 60°.

Moreover, we studied the the reflection characteristics for different random layer arrangements by keeping the total number of layers constant at 64 in all simulations. We use the randomness formulation of $H(i) = (1+r)\bar{H}[1+r_1(i)]$ and $L(i) = (1-r)\bar{L}$ [76], where r is the inhomogeneous parameter, the term $1 + r_1(i)$ is a random factor added to high refractive index material thickness, $H(i)$ and $L(i)$ represent the thickness of high and low refractive index in the i^{th} layers respectively. Similarly, $\bar{H} = \lambda_0/4\eta_h$ and $\bar{L} = \lambda_0/4\eta_L$, where λ_0 is the center wavelength of 550 nm; η_H and η_L represent the index of the high and low refractive index materials respectively. The first randomness is generated by using $r = 0$ and $r_1 = 0$. This choice is equivalent to a 64 layer quarter wave alternate high and low index structure. Similarly, a second randomness experiment is simulated by $r = 0.1$ and $r_1 = 0$, we found slightly better reflection performance.

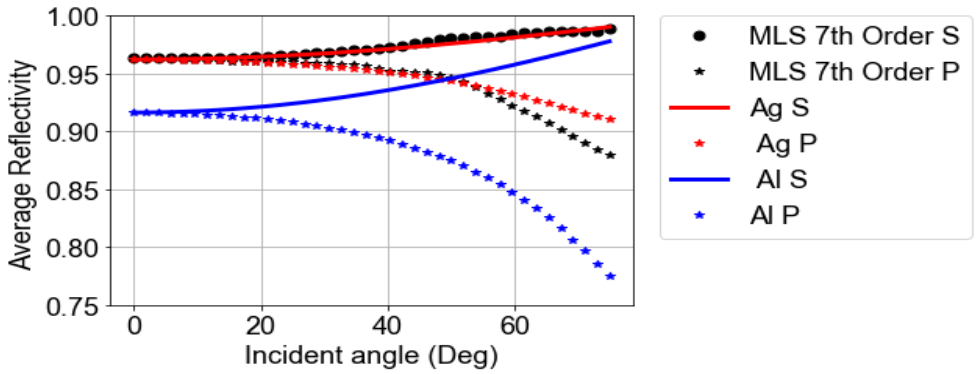

Figure 19: Average reflection as function of incident angle in visible frequency region for 7^{th} order ($N = 7$) MLS and metallic reflectors for both s- and p-polarized light.

Table 6: Average reflection coefficient for different random order multilayer structures.

Incident angle(deg)	Random 1	Random 2	Random 3
0	0.7936	0.8694	0.8616
30	0.8217	0.9017	0.8823
60	0.8789	0.9630	0.9574

Finally, extensive randomness is generated by varying the $r_1 i$ as: 0.005,0.01, 0.015, 0.020,0.025, 0.030, 0.033, 0.036, 0.039, 0.042, 0.045, 0.048, -0.048, -0.045, -0.039, 0.036,-0.033, -0.030, 0.025,-0.020, -0.017, -0.014, -0.011, -0.008, -0.005,-0.002, 0.048, 0.045, 0.042, 0.039, 0.036, 0.033. Table 6 summarizes the average s-polarized reflectivity for these three different random order inhomogeneous multilayer structures. The average reflectivity for 7^{th} order MLS illustrated in the first column of Table 4, has higher average reflection than those of these different random layer multilayer structures.

The average reflectivity for 7^{th} order MLS has higher average reflection than those of these different random layer multilayer structures.

Clearly, the parameter space of random multilayers is very large and it is not easy to exhaustively search this space. However, to make a broadband reflector that works at all

angles, the key factor is the existence of a wide range of periodic high-low index transitions of uniform amplitude. The Fourier spectrum of the transitions of such a system would be broad and flat. The MLS sequence is deterministic and possesses these characteristics in a mathematically perfect way. It was this characteristic of MLS sequences that led to the design and demonstration of acoustic grating diffusers [75], one of the earliest applications of the MLS.

Table 7: Average reflection coefficient in visible frequency range for 6^{th} order MLS designed using different materials.

Incident angle(deg)	GaP/MgF_2(2.493)	ZnS/Cryolite(1.76)	ZnS/MgF_2(1.72)
0	0.9983	0.9619	0.9522
30	0.9987	0.9689	0.9514
60	0.9998	0.9926	0.9896

Finally, the reflection characteristics of a multilayer depends on the refractive index contrast ratio of the high index material to the low index material. Higher contrast ratio leads to better reflector performance. We analyze the reflection characteristics for commonly used refractive index materials such as ZnS(2.3862) -MgF_2(1.384) and ZnS(2.3862)- Cryolite(1.33). Table 7 illustrates the average reflection coefficient over a broad range of incident angles in the visible frequency regime for 6^{th} order ($N = 6$) MLS multilayer structure design using these different dielectric materials. The MLS multilayer design with GaP(3.31) -MgF_2(1.38), having refractive index contrast ratio of 2.493, has higher reflection (more than 99%) than any other material for all ranges of incident angles. For the wave incident at 0°, the GaP -MgF_2, ZnS-Cryolite, and ZnS -MgF_2 with refractive index ratio 2.493, 1.76, and 1.724 has reflection of 99.83%, 96.19%, and 95.22% respectively.

Table 8: Different multilayer structure.

Structure	Sequence	Spectrum	Substitution rule
MLS	Periodic	continuous	$S_{k+3} = S_{k+1} \oplus S_k$
Fibonacci	Deterministic, aperiodic	pure point	$A- > AB, B- > A$
Thue-Morse	Deterministic, aperiodic	Singular continuous	$A- > AB, B- > BA$
Rudin-Shapiro	Deterministic, aperiodic	continuous	$AA- > AAAB, AB- > AABA,$ $BA- > BBAB, BB- > BBBA,$

Table 9: First four sequence generation for different aperiodic structures.

Sequence(S_k)	Fibonacci	Thue-Morse	Rudin-Shapiro
S_0	A	A	AA
S_1	AB	AB	$AAAB$
S_2	ABA	$ABBA$	$AAABAABA$
S_3	$ABAAB$	$ABBABAAB$	$AAABAABAAAABBBAB$

However, the different symbolic substitution and repetition rules has been employed to produce deterministic aperiodic multilayer structures too. The pure point or continuous Fourier spectra of these aperiodic structures (especially the Rudin-Shapiro) are important for comparative analysis with the MLS multilayer periodic continuous spectrum.

Table 10: Average Reflection coefficient over the visible frequency range for different aperiodic multilayer structure.

Incident Angle(deg)	Fibonacci(34)	Thue-Morse(32)	Rudin-Shapiro(32)
0	0.8174	0.6914	0.8445
15	0.8299	0.6836	0.8531
30	0.8715	0.7118	0.8734
45	0.9137	0.8001	0.9013
60	0.9432	0.8839	0.9317
75	0.9674	0.9373	0.9488

The Fibonacci, Thue-Morse, and Rudin Shapiro substitution rules are commonly used

substitution used in multilayer aperiodic photonics quasi crystals design [80,81]. In Fibonacci substitution rule $A- > AB, B- > A$ and further with first sequence with A, can be extended as $A- > AB- > ABA- > ABAAB- > ABAABABABA- > ABAABABAABAAB- >$ .... Similarly, the Thue-Morse grating structure is determined using the rule $A- > AB, B- > BA$ and the Rudin Shapiro by $AA- > AAAB, AB- > AABA, BA- > BBAB, BB- > BBBA$ [82, 83]. All these substitution rules for the first four sequence generations is summarized in Table 8 and 9. The practical implementation of such structures is to replace each letter by either a high or a low refractive index material layer [84].

Table 10 illustrates the average reflection coefficient over the visible frequency range for different aperiodic multilayer structures. For the wave incident at 0°,the Fibonacci, Thue-Morse and Rudin-Shapiro structures have reflectivities of 0.8174, 0.6914, and 0.8445 respectively. Similarly, we found the higher reflectivity for the wave incident at 60°, with values of 0.9674, 0.9373, and 0.9488 for the Fibonacci, Thue-Morse and Rudin-Shapiro structures respectively. Further, these values are less than the 99.03% and 96.22% reflection for light at normal incidence respectively for aluminum and silver metallic reflectors. Clearly, the metallic and MLS reflectors have higher reflectivity compared to aperiodic multi-layer structures.

Figure 20 illustrates the graphical representation of the reflection characteristics for Fibonacci and Rudin-Shapiro multilayer structures for s-polarized light incident with 0°, 30°, and 60° respectively. The Rudin-Shapiro multilayer structure has better reflection in range of 500 nm to 650 nm at most incident angles compared to the Fibonacci structure. However, due to Fourier spectral difference, the Fibonacci structure has slightly higher average reflection (nearly 2% more) than Rudin-Shapiro for all visible frequencies.

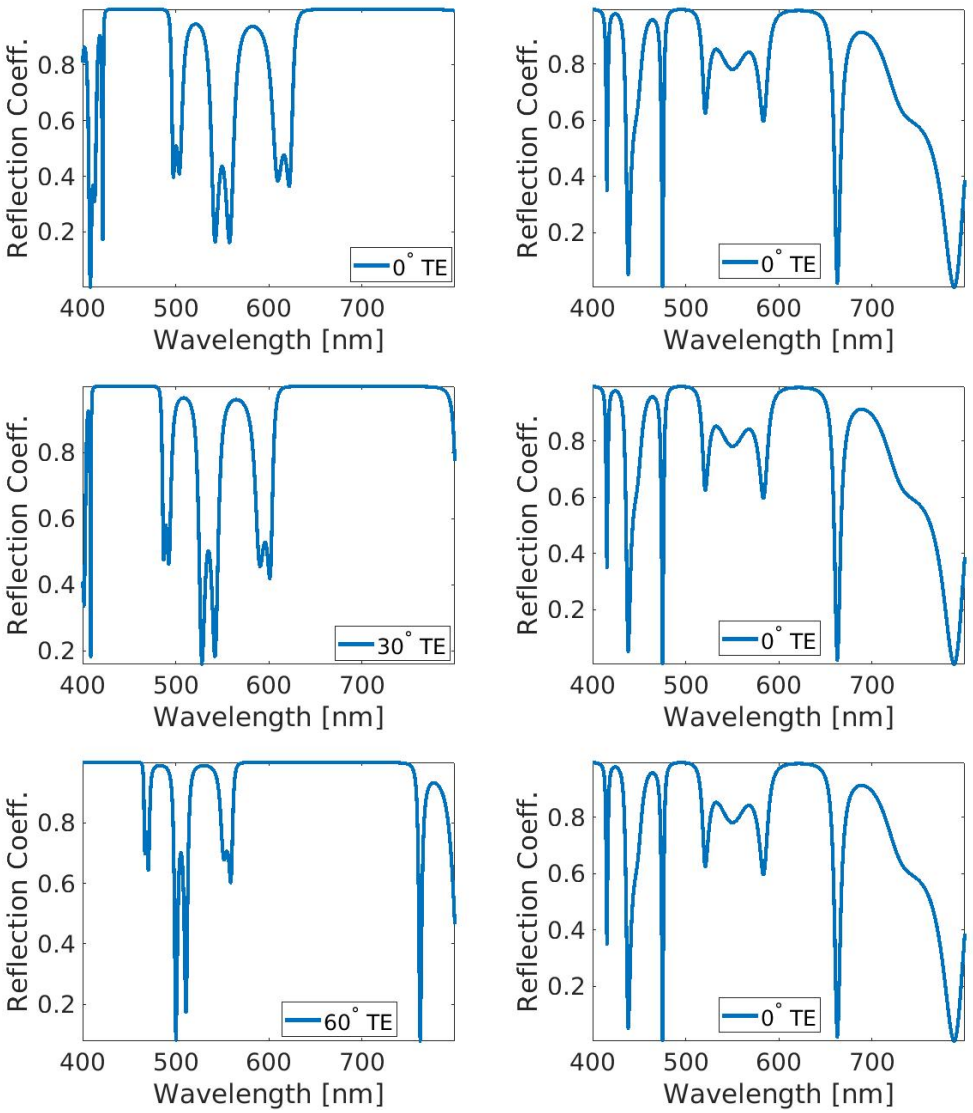

(a) Fibonacci (b) Rudin-Shapiro

Figure 20: Reflection characteristics for Fibonacci and Rudin-Shapiro multilayer structure for s- polarized light incident with 0°, 30°, and 60° respectively.

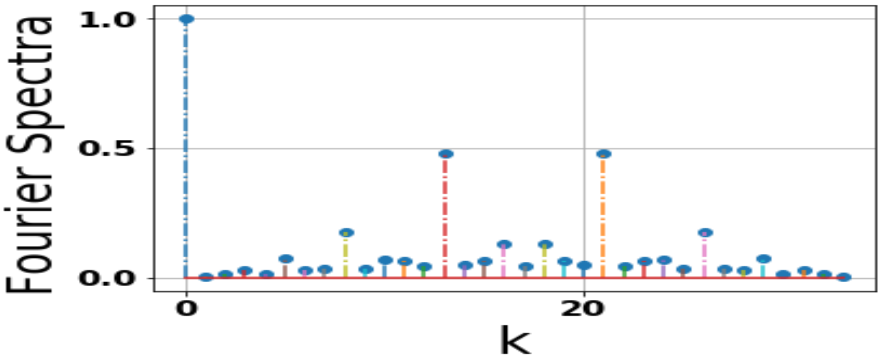

Figure 21: Spectral characteristics of Fibonacci aperiodic structure.

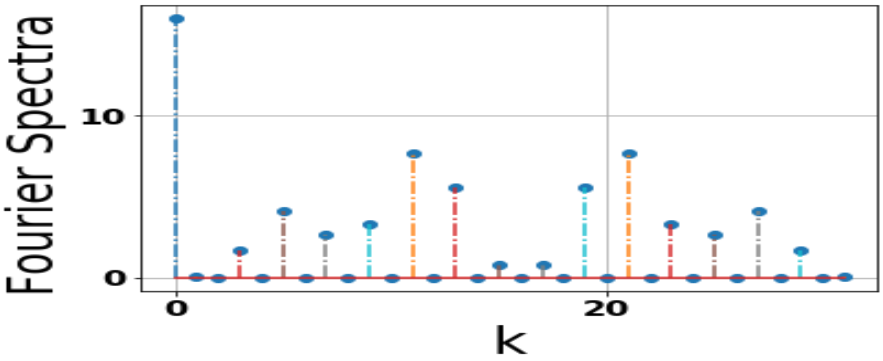

Figure 22: Spectral characteristics of Thue-Morse aperiodic structure.

The approach to generate deterministic aperiodic structures with controlled Fourier spectral properties relies on symbolic substitu tions [80, 109]. The Fibonacci has a deterministic and aperiodic sequence with pure point spectrum. The pattern for a Fibonacci structure with 34 layer and order 7 is ABAABABAABAABABAABABAABAABABAABAAB. The Figure 21 illustrates the spectral characteristics of Fibonacci aperiodic structure. Similarly, both of the Thue-Morse and Rudin-Shapiro are deterministic and aperiodic sequence structures. However, the Thue-Morse has a singular continuous spectrum and the Rudin-Shapiro has continuous spectrum. Figure 22 shows the spectral characteristics of 32 layer and 5 order Thue-Morse aperiodic structures with a pattern of ABBABAABBAABABBABAABAB-BAABBABAAB. Similarly, Figure 23 shows the spectral characteristics of Rudin-Shapiro

aperiodic structure.

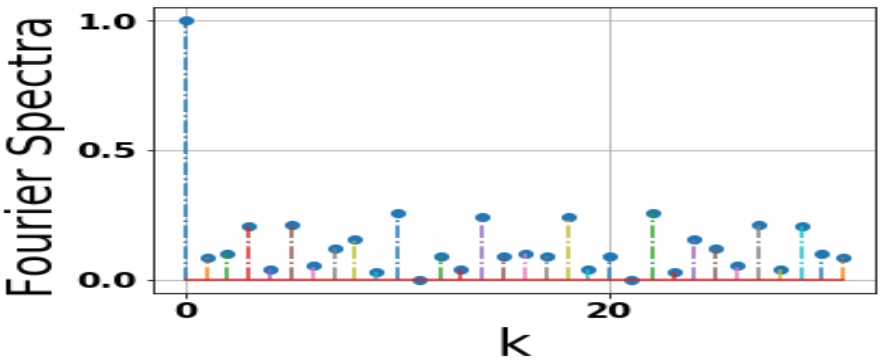

Figure 23: Spectral characteristics of Rudin-Shapiro aperiodic structure.

Another way to look the reflection characteristics is to analyze the color spectra of maximum length sequence and compare that with alternate multilayer structures. The reflection equivalent spectrum plot for MLS by using Python ColorPy and tmm packages is illustrated in Figure 24. The ColorPy is a Python package to convert physical descriptions of light spectra of light intensity vs. wavelength into RGB colors that can be drawn on a computer screen. It provides a nice set of attractive plots that you can make of such spectra, and some other color related functions as well.The amount of light intensity for each wavelength is the same. But since the human eye has different sensitivity to different wavelengths, the apparent brightness looks different for different colors. For example, the color for 750 nm is quite dark, while the color for 550 nm is quite bright [6].

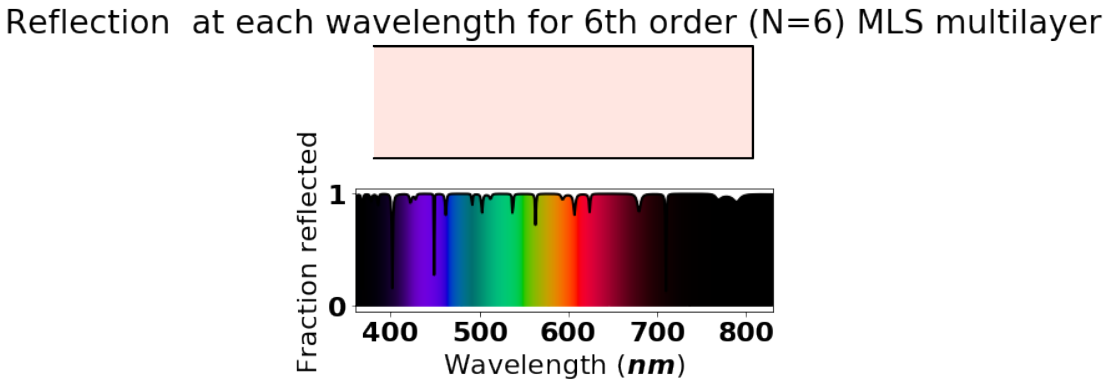

Figure 24: Color Spectral characteristics of Maximum Length Sequence structure.

Similarly, Figure 25 shows the spectral reflection characteristics for 32 layer alternate high and low multilayer structure. We found very good reflection over the visible frequency spectrum for for 6^{th} order ($N = 6$) MLS multilayer structure design using these different dielectric materials compared to 32 layer alternate high and low refractive index multilayer structure.Thus, this is one of the nice way to differentiate the reflection characteristics for different incident angle with the help of overall color spectra as in color spectroscopy techniques.

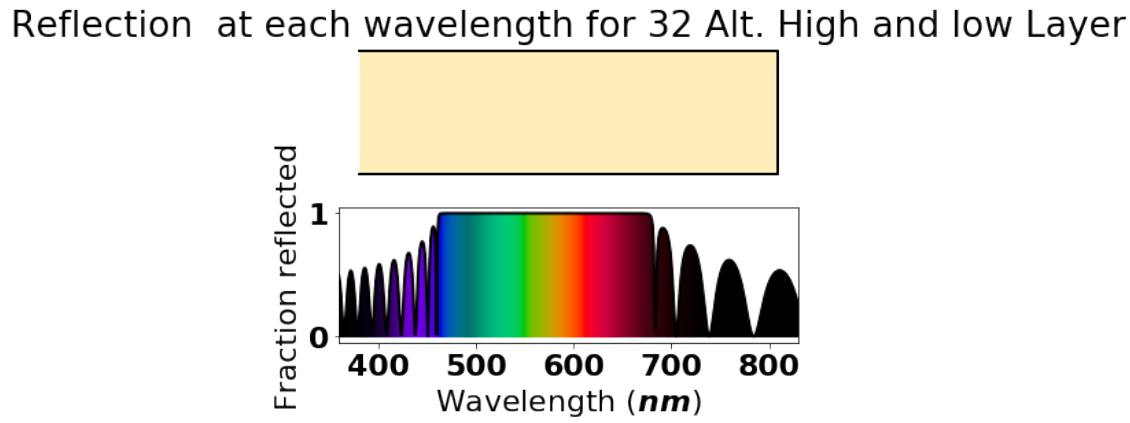

Figure 25: Color Spectral characteristics of Rudin-Shapiro Alternate high and low 32 layer structure.

3.3 Summary

This work has explored the reflection performance of MLS multilayer structures at visible wavelengths. The MLS system is an aperiodic system that has been little studied for applications in optics. It is a system that is ripe for investigation as a medium to support optical localization and surface waves, and as an ultra-wide photonic band gap material in two and three dimensions. The wide range of periodicities contained in an MLS structure leads to broadband reflection characteristics for all incident angles. The analysis here shows that multilayers with an MLS profile can function as effective omni-directional reflectors. The narrow reflectivity dips mean that such reflectors would not be good for monochromatic laser reflection but rather for incoherent broad bandwidth light. The comparative analysis presented was made both to periodic multilayers and to the metallic reflectors silver and aluminum, whose refractive index was modeled based on the Brendel-Bormann (BB) model in the visible frequency region. We demonstrated broadband reflection for the MLS multilayer design by varying the number of layers or the refractive index of the constituent layers. Further, the average reflection characteristics for other aperiodic structures using Fibonacci, Thue-Morse, and Rudin Shapiro substitution rules also demonstrated and compared the simulated results. Finally, the attractive color spectra of maximum length sequence and alternate multilayer structures has obtained for visible frequency ranges.

CHAPTER 4

BLOCH SURFACE WAVE EXCITATION USING A MAXIMUM LENGTH SEQUENCE GRATING

4.1 Introduction

This paper presents simulations of a method of coupling to Bloch Surface Waves (BSWs) using maximum length sequence (MLS) gratings on the top of multilayer photonic band gap structures. An MLS grating has a superposition of a wide range of periodicities which should permit coupling of a broad angular range of monochromatic light or a wide spectral range of collimated light into Bloch surface wave on a photonic band gap multilayer. This paper presents the details and results of this novel grating coupling technique including finite-element-method calculations of the E-field profile and a mathematical analysis of phase matching criteria.

Bloch Surface Waves (BSWs) supported by one-dimensional photonic crystals are electromagnetic modes that propagate along the interface of a truncated dielectric multilayer structure and a homogeneous medium. In terms of dispersion relation, evanescent field profile, and optical coupling requirements, BSWs can be considered as an analog of surface plasmon-polariton (SPP) generation in metals. Theoretical and experimental studies have been carried out on BSWs [7, 8] and this optical excitation is naturally suited for a broad range of applications in photonics including label-free bio-sensing [10], surface enhanced Raman spectroscopy [11], optical slow-light devices [14], florescence based detection [15], and slot waveguides [**?**, 16, 30, 88–90]. Further, recent research has investigated the BSWs properties for integrated circuits [9], optical fiber tip [12], and radiation continuum modes [13]. The breadth of applications is due to the flexibility in operating wavelength range, easy experimental realization, larger figure of merit (FOM), and robustness in many sensing applications. SPP's, despite their widespread application, are significantly restricted by the

high ohmic loss inherent in metals that results in resonance broadening and a reduction both in surface field enhancement and in sensing FOM.

BSWs are non-radiative excitations that require a phase matching mechanism to couple to light. Most methods are based on evanescent prism-coupling, either in the Kretschmann or Otto configurations. Coupling to BSWs through the use of a grating profile on the top of the active medium is an attractive alternative because it eliminates bulky prism requirements [17]. In both prism and grating coupling, the incident light is coupled into a surface mode of the structure only when the parallel-wave-vector phase matching condition is satisfied [18]. It is the sensitivity of the phase-matching characteristics to surface conditions that makes possible BSW-based sensors for label-free detection including DNA-probe binding, protein aggregation, antigen-antibody reaction, and many more. Both prism and periodic gratings only provide coupling over a single narrow angular range for incident monochromatic radiation. The motivation for this study [91] was that an MLS grating profile should permit coupling at multiple angles of incidence because the MLS sequence contains a broad spectrum of grating profiles of equal amplitude. The effective surface roughness of an MLS grating grows as the order of the MLS sequence increases. In a similar vein to the work described here, the effect of surface roughness on solar cell design to improve the overall optical characteristics has been an important research concern for solar researchers and scientists [92]. The better light trapping and absorption in solar cells can be achieved by designing front and back textured surfaces.

4.2 MLS Grating Model

When a plane electromagnetic wave is incident on a periodic diffraction grating structure at an angle of θ, the incident wave intensity is split into diffracted, reflected, or transmitted components. The diffraction wavefronts can be found for wavelengths short compared to grating period (Λ). The optical path difference of transmitted diffracted wavefront for

positive interference can be expressed in terms of integer multiple of wavelengths [29].

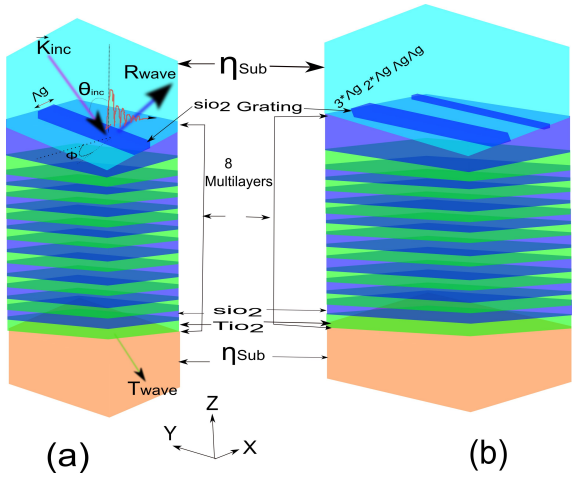

Figure 26: Multilayer design with grating defined by (a) Periodic structure (b) MLS structure at the top of multilayer

Mathematically,

$$m\lambda = \Lambda(\eta_{II} sin\beta_m - \eta_I sin\theta) \tag{91}$$

where η is refractive index of each medium,$m = ..., -2, -1, 0, +1, +2....$ are the diffraction orders and β_m is the transmitted diffracted beam angle. For $m = 0$, the angle of refraction, β_0 described by Snell's law as,

$$\beta_0 = \arcsin(\frac{\eta_I}{n_{II}}) sin\theta \tag{92}$$

The maximum values of the sine function varies between -1 and 1. Thus,the higher order diffraction order satisfies the condition

$$-(\eta_I + \eta_{II}) < \frac{m\lambda}{\Lambda} < ((\eta_I + \eta_{II}) \tag{93}$$

The extended criteria for non-transmitted diffracted beam of order of 2 or more is

$$\frac{2\lambda}{\Lambda} > (\eta_I \mid sin\theta \mid) + \eta_{II}) \tag{94}$$

Similarly, the optical path difference of reflected diffracted wavefront for positive interference can be expressed as,

$$m\lambda = \Lambda(\eta_I sin\theta_m - \eta_I sin\theta) \tag{95}$$

where the θ_m is the reflected beam of diffraction order m. For specular reflection with m=0,

$$sin\theta_0 = sin\theta \tag{96}$$

The additional defect layer at the top of multilayer structure acts as a suitable active medium for Bloch surface waves [7]. A grating on top of this terminating layer eliminates the need of a bulky prism configuration. The grating profile couples the incident plane wave into the surface mode of photonic crystal when the parallel momentum phase matching criteria is satisfied [18]. The phase matching criterion can be expressed as

$$k_{BSW} = k_0 \eta_{sup} sin(\theta_{inc}) + \frac{2\pi m}{\Lambda_g} \tag{97}$$

where k_{BSW} is BSW wave vector, $k_0 = \frac{2\pi m}{\lambda_0}$ is free space wave vector,η_{sup} is the refractive index of superstrate, θ_{inc} is the incident angle, m is an integer, and Λ is the grating period. For a given wavelength λ, m=1 and $\theta_{inc} > 0$, the BSW can only be excited when the grating period Λ_g satisfies the condition of $\frac{\lambda}{\Lambda} < \frac{k_{BSW}}{k_0} + 1$.Thus, the grating periods are in the range of $\frac{k_{BSW}}{k_0} < \frac{\lambda}{\Lambda} < \frac{k_{BSW}}{k_0} + 1$.

The k_{BSW} for the multilayer only with prism configuration can be expressed as

$$k_{BSW} = k_0 \eta_{sup} sin(\theta_{res}). \tag{98}$$

We assume that using same k_{BSW} in equation 2 exactly matches the k_{BSW} of the multilayer with prism configurations. The total k_{BSW} in grating design is the sum of K_{inc} and k_g. The appropriate selection of Λ_g can produce the broadband coupling of BSW wave through the multilayer structures.

This grating can be designed using periodic or aperiodic surface profiles. Here, we design the grating structure using a maximum length sequence profile. A MLS is a pseudo random binary sequence (PRBS) generated by a cyclic shift of m-sized linear feedback shift registers (LFSR) [95]. Computationally, these sequences can be generated using the recursive formulation $S_{k+3} = S_{k+1} \oplus S_k$. Here, the $\oplus$ symbol represents XOR (modulo-2 sum)

operation.The MLS sequences produce a flat frequency response, a feature that is used in the acoustic impulse and spread spectrum communication applications.

Table 11: MLS generation for N=3.

Step(k)	S_2	S_1	S_0	S_k
0	A	A	A	A
1	B	A	A	AA
2	B	B	A	AAA
3	A	B	B	$AAAB$
4	B	A	B	$AAABB$
5	A	B	A	$AAABBA$
6	A	A	B	$AAABBAB$
7	A	A	A	$AAABBAB$

Table 11 shows the $N = 3$ sequence generated using this formulation. Each letter **A** and **B** in Table 11 represents 1 (higher) and 0 (lower) refractive index material. The thickness of grating profile is defined by the MLS sequence. To convert to multilayer thicknesses the A and B correspond to the two different refractive index materials. Thus, the final sequence for N=3 can be expressed as [3 2 1 1] [30]. Figure 26 shows the design of a periodic and a order 3 MLS multilayer design. The periodic structure in figure (a) includes the substrate of 8 alternate multilayer of SiO_2 and TiO_2 along with grating on top of multilayer. Similarly, the MLS grating profile is on top of an identical multilayer. The superstrate material refractive index is varied from 1.3280 to 1.33 and the substrate material SiO_2 is wavelength dependent refractive index material.

The main goal of the this research is to show the multiple wavelength coupling by grating design. However, sometime it is worth to show the sensitivity analysis for sensing application. Therefore, the angular sensitivity of the Bloch surface wave defined as the ratio of change in resonance angle to change in refractive index. Mathematically, the angular sensitivity can be defined as

$$S_\theta = \frac{\Delta\Phi}{\Delta\eta}, \tag{99}$$

where $\Delta\Phi$ is the change in BSW resonance angle and $\Delta\eta$ is the refractive index change.

Similarly, the spectral sensitivity is defined as the ratio of change in wavelength to change in refractive index as

$$S_\lambda = \frac{\Delta\lambda}{\Delta\eta}, \tag{100}$$

where $\Delta\lambda$ is the change in BSW resonance wavelength and $\Delta\eta$ is the change in refractive index. As we noticed that the the change in refractive index and shift in resonance has important effect on biosensor, we introduce a figure of merit (FOM) at BSW resonance, which is defined as

$$FOM = \frac{S_\theta(1 - MRR)}{FWHM}, \tag{101}$$

where MRR is the minimum reflection at resonance, (1-MRR) represents the depth of resonance and FWHM is the full width of resonance dip at half-minimum. So, this can be written as

$$FOM = \frac{S_\theta D}{W}. \tag{102}$$

. The change in refractive index also generates the change in intensity at resonance angle. The Figure 33 shows the change ΔR due to refractive index variation $\Delta\eta$ as

$$\Delta R = \frac{dR}{d\theta}\frac{d\theta_{BSW}}{d\eta}, \tag{103}$$

where $S_{theta} = \frac{d\theta_{BSW}}{d\eta}$ is the sensitivity defined by equation 1 and $\frac{dR}{d\theta}$ is the slope of the resonance at any point [96]. The narrower and deeper the BSW resonance has higher FOM, so the more accurate detection of biosensing analyte is possible. The detection accuracy (DA) is defined as.

$$DA = \frac{1}{FWHM}. \tag{104}$$

Further, we can express the relationship between parallel wave vector of the BSW, and the the refractive index of the prism as

$$k_{BSW} = \frac{2\pi}{\lambda_{BSW}}\eta_{sup} sin(\theta_{BSW}) \tag{105}$$

where k_{BSW} is the parallel wave vector of the BSW, η_{sup} the the refractive index of the prism,θ_{BSW} and λ_{BSW} are the incident angle and wavelength at minimum reflectively at

resonance point. The change in angular frequency and parallel wave vector might change the overall dispersion characteristics and can be useful to calculate the overall group velocity v_g, which is slightly less than speed of the light in the medium.

$$v_g = \frac{\delta\omega}{\delta k} \tag{106}$$

where k is the parallel wave vector of the BSW, and ω is the angular frequency.

4.3 Results and Discussion

When an electromagnetic wave is incident on the the multilayer structure with a grating defined by MLS structure, Bloch surface wave generation can occur.In the computational simulation described here, thickness of TiO_2 and SiO_2 layers were chosen to be 126.1 nm and 205.41 nm respectively. One additional SiO_2 defect layer of thickness 280.3 nm is added at the top of this multilayer in between the superstrate and the topmost TiO_2 layer. The high refractive index, TiO_2 and low refractive index, SiO_2, materials are picked in our design due to their deposition compatibility and frequent use in dielectric multilayer films.The refractive index of TiO_2 and SiO_2 layers at a wavelength of 700 nm, are 2.5512 and 1.4553 respectively. Figure 27 and 28 shows the wavelength dependent refractive index characteristics of TiO_2 and SiO_2 materialS [93,94]. The BSW reflection on the surface of one dimensional multilayer structure is highly dependent on the thicknesses of the periodic multilayer and that of the defect layer. For the periodic grating, the grating period (Λ_g) is set to 1920 nm and the grating depth is 70 nm with fill factor of 0.5. The groove width also determined the fill factor(ff). Usually, we select a fill factor around 0.5 in periodic grating design for symmetry of multiple periods. The index of the superstrate layer (η_{sup}) is varied from 1.3275 to 1.3300 in our simulations. For the MLS structure, the grating surface profile is defined by using the MLS sequence of [3 2 1 1] with alternate SiO_2 and superstrate material. More specifically, the pattern is $3 * \eta_{SiO_2}$, $2 * \eta_{sup}$,$1 * \eta_{SiO_2}$,$1 * \eta_{sup}$. Now, this grating on the top of multilayer

mediates the coupling of light into Bloch surface mode without use of a bulky prism and that satisfies the condition given by Equation 97. We presume, $\eta_{sup} = 1.33$, $m = 1$, $K_0 = \frac{2\pi}{\lambda}$ and $\Lambda_g = 400nm$. Equation 97 provides the resonance angles of 16.634, 22.355 and 36.22 degrees for grating period of Λ_g, $2 * \Lambda_g$, $3 * \Lambda_g$.

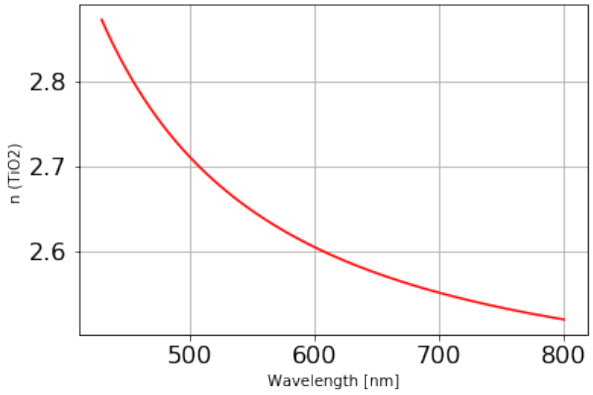

Figure 27: Wavelength dependent refractive index characteristics of TiO_2 material [93].

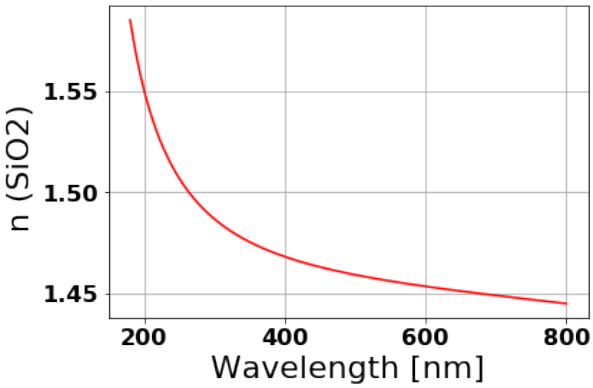

Figure 28: Wavelength dependent refractive index characteristics of SiO_2 material [94].

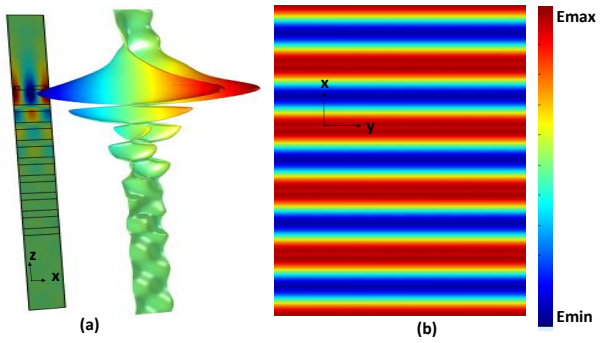

Figure 29: BSW E-field of y component in (a) xy (b)xz plane.

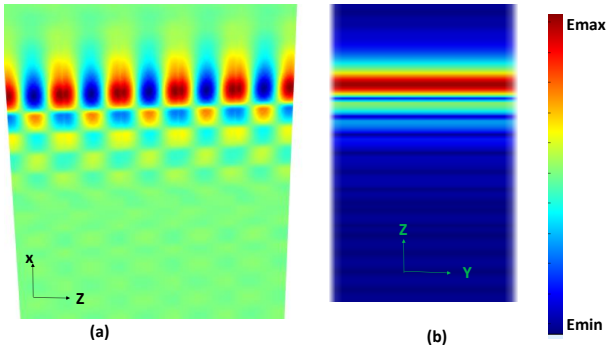

Figure 30: BSW E-field of y component in (a) xz (b) BSW normalized E-field of y component in zy plane.

Figure 29 (a) and (b) illustrates the BSW electric field profile for E_y at wavelength of 632.8 nm along xy and yz planes respectively. Further, Figure 30 (a) and (b) shows the BSW electric field profile for E_y along xz and normalized electric fields along yz planes at wavelength of 632.8 nm and refractive index of 1.33. The BSW modes electric fields are highly confined on the surface of the grating structure in all of these different cases.

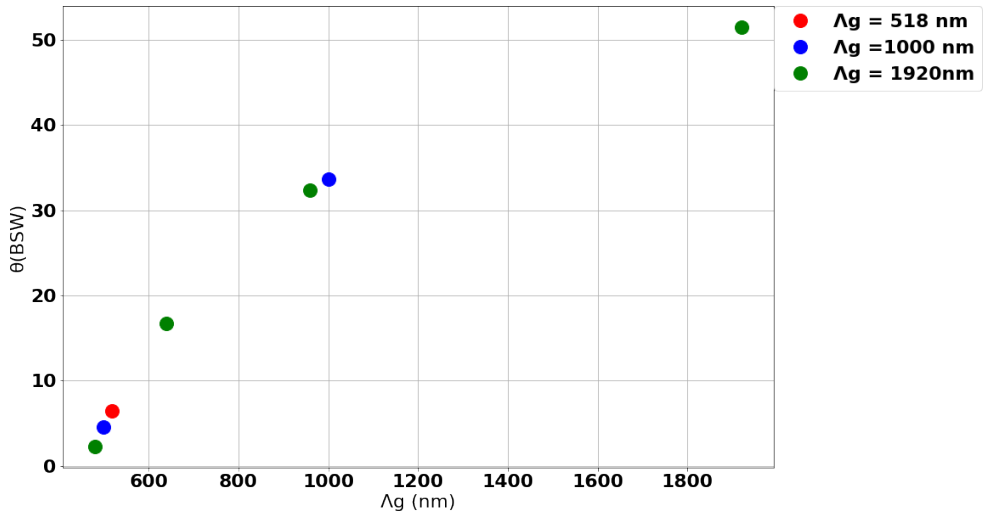

Figure 31: The variations of BSW angles for different value of grating period.

Figure 31 demonstrates the variations of BSW angles for different value of grating period. We found the resonance angle of 10.33°, 27.10°,and 47.03° for the grating period of 1920 nm. Similarly, we observe 10.33°, and 27.10° for the grating period of 1000 nm and 10.33° for the grating period of 518 nm.

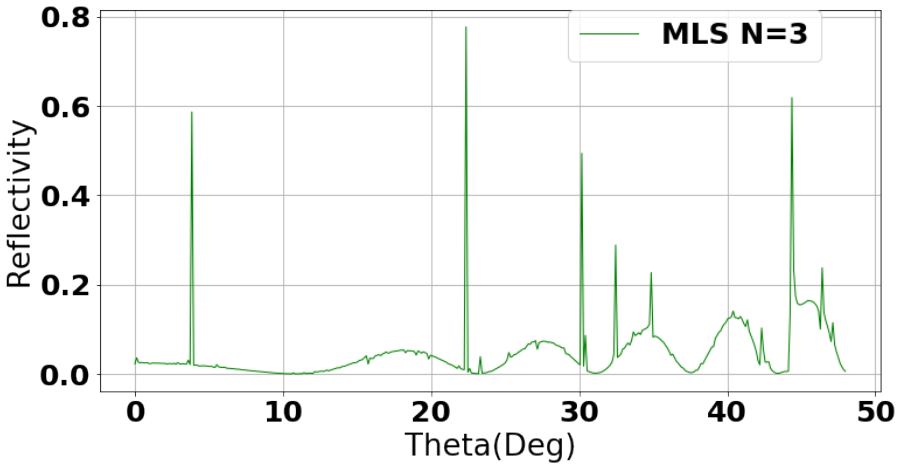

Figure 32: Reflectivity characteristics as function of incident angle for MLS with N=3.

Figure 32 illustrates the reflectivity characteristics curve as function of incident angle (θ). We can observe the BSW coupling at the resonance angle of 7°, 26°, 30°, and 47°.

This proves the broad angle coupling of MLS BSW into multilayer structure. These values are almost similar to the value obtained from the mathematical equation of phase matching for grating coupling. The resonance angle of phase matching can be expressed as $\theta_{BSW} = sin^{-1}(K_{BSW} - K_g)/(k_0 * \eta_{sup}$, where K_g is the grating wave vector that can be expressed as $2 * \pi * m/\Lambda$. By using this mathmatical expression for MLS with $N = 3$, we can get positive resonance angles of 10.33°, 27.10°, and 47.03°. We are able to get almost a close match between the mathematical and simulated values. These values are obtained from the COMSOL Multiphysics simultion along with 16 layer alternate TiO_2 and SiO_2 layers having grating period of 1920 nm and a operating wavelength of 700 nm. The slight variation in simulation might be due to meshing size, step size selection, wavelength dependent dielectric refractive indices, mathematical precision point and others parametric selection in COMSOL MultiPhysics simulations.

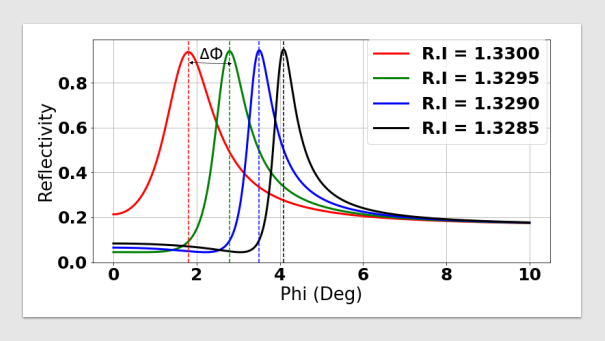

Figure 33: function of incident azimuthal angle for different values of n_sup.

Table 12: BSW coupling angles for various orders of MLS grating

MLS ($order$)	Coupling Angles(θ)
3	7°, 26°, 30° and 47°
4	6°, 22°, 30°, 31°, and 45°
5	10°, 15°,21°, 30°, 39°,46°, and 48°

Figure 33 shows variation in the BSW reflectivity resonance angle as the refractive index of super-strate is changed from 1.3285 to 1.3300. We found the broader range of azimuthal

angles for higher refractive index value. The reflectivity curve becomes narrower for decreasing refractive indices even though resonance occurs at a higher value of azimuthal angle. The maximum sensitivity of 3000 degree per refractive index unit (deg $/RIU$) can be achieved by using this multilayer setup for refractive index changes from 1.3295 to 1.3300($\Delta\eta = 0.0005$). The corresponding peaks in the reflectivity show high- confined, narrow surface waves for the values are only sensitive to the design parameters. Table 12 illustrates the BSW coupling angles for various orders of MLS grating. We can observe higher angle coupling for higher order MLS. Further, if we design the grating structure with higher number of MLS orders, we can couple broad angular range of monochromatic light or a wide spectral range of collimated light into Bloch surface wave on a PBG multilayer. The ability to simulate higher gratings is limited by the size of simulation that can be done in COMSOL.

4.4 Summary

This research presents a exploration of the excitation of Bloch surface waves in dielectric multi-layers with MLS grating structures on top most layer. This MLS, an aperiodic system contains wide range of periodicities leading to broadband coupling of monochromatic light or wide spectral range of collimated light into Bloch surface wave on multilayer. The comparative analysis presented was made both to periodic and MLS grating profile. Our study of this idea believes that the possibility of more sensitive as well as broader Bloch surface wave coupling can be realized compared to a periodic grating counterpart. The detailed analysis of the surface electric field and angular sensitivity provides the better understanding of BSW grating coupling.

CHAPTER 5

OTHER RELATED APPLICATIONS

5.1 Frequency Selective Surfaces for Microwave Frequency Band Applications

In recent years, the advent of frequency selective surfaces (FSSs) for microwave/millimeter wave applications have attracted a lot of attention for applications such as polarizers, absorbers, radomes, and reflectors. FSSs are two dimensional periodic structures like 2-D photonic band-gap materials, designed to transmit, reflect, or absorb particular frequencies of electromagnetic waves. FSSs have been designed and implemented using different techniques and unit cell structures. Based on the application and resonance frequency, the split ring resonator (SRR), complementary split ring resonator (CSRR), cross structure, and rectangular SRR are used to design FSSs. FSSs are commonly used in microwave and millimeter wave applications due to small unit cell compared to wavelength and strong electric or magnetic current near resonance. Thus, based on diffraction theory, the secondary grating lobes are suppressed with no coupling between adjacent elements. It was proved using Babinet's principle in [103], that the SRR acts as band-stop filter while CSSR acts as band-pass filter with very narrow-band characteristics. Further, the multilayer structure of such elements or single layer dielectric thickness variation helps to create high Q-factors and narrow filter pass bands. Pendry demonstrated the use of left handed materials (LHMs) that exhibit negative permeability near magnetic resonance [105]. Smith realized such meta-materials using one or two-dimensional periodic SRR structures [106]. Meta-materials are sub-wavelength periodic structure that are engineered to produces exotic electromagnetic behavior not found in nature. For SRR, the broadband negative permeability is implemented by using equivalent gap capacitance and negative permittivity by shunt inductance. In contrast, for CSRR, the equivalent dual counterpart of SRRs, is fabricated using a negative image of SRRs [103].

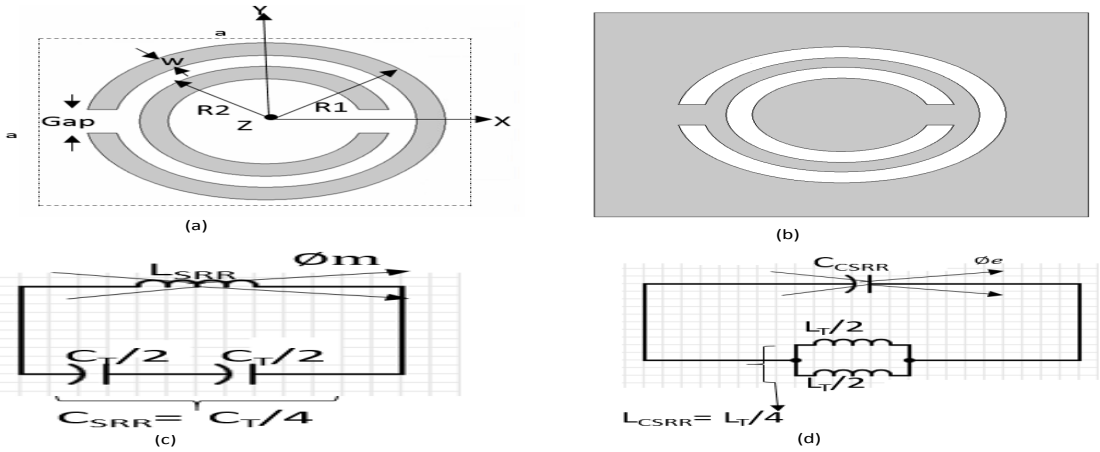

Figure 34: The FSS unit cell structure of (a) SRR (b) CSRR with grey part copper metal as PEC and white portion Alumina ($\epsilon = 9.8$) as substrate. The geometrical parameters are a=15mm, R1=5mm, R2=3.5mm, Gap=1.5mm, w=0.8mm. (c) The equivalent LC circuit for SRR (d) for CSRR.

Due to low loss, two-dimensional dielectric FSSs or low loss metallic photonic crystals at optical wavelengths are used extensively in applications. This paper explores the design of FSSs using high permittivity alumina as the substrate. Alumina has a high dielectric constant, low dielectric loss, and high electric/ heat resistance [104]. The comparative analysis of different parameters for SRR structure provides the best transmission throughput at the desired frequency band. Invisibility cloaks, super-lensing, negative refraction, diffraction limited image resolution, and massive MIMO antenna design are recent research breakthrough examples using such meta-materials or meta-surface structures [88].

The unit cell of SRRs and CSRRs with double concentric rings and opposite gaps are depicted along with equivalent circuits in Fig. 34. When SRRs is excited by an external magnetic field parallel to the SRR axial direction, the magnetic dipole is created due to magnetic loop [103]. Therefore, the presence of equivalent loop inductance and gap capacitance shows strong Lorentzian resonance in the effective permeability. The capacitive contribution of the inner ring reduces the overall resonance frequency and tries to make more homogeneous to

electromagnetic excitation by adjusting the wavelength and lattice constant ratio [105]. In

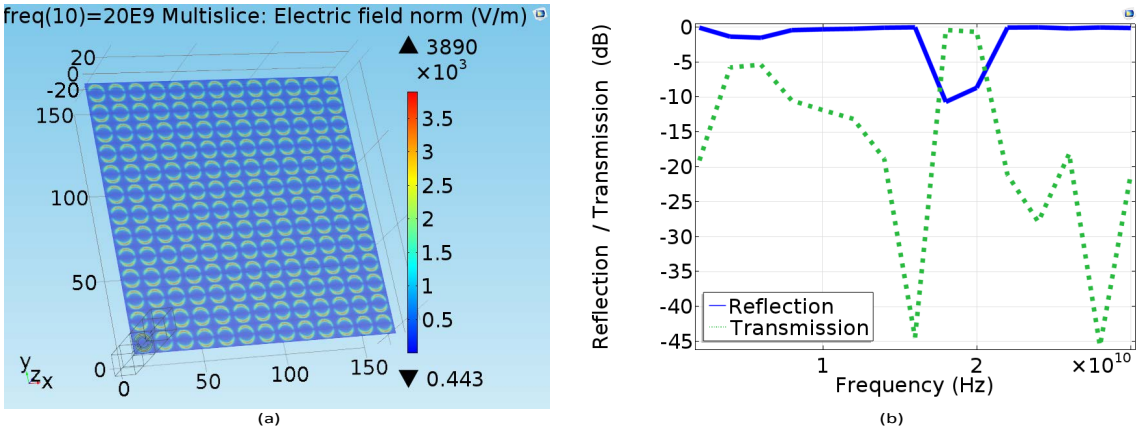

Figure 35: (a) 13× 13 FSS model (b) Trasmission and reflection characteristics for unit cell of FSS.

Fig. 34 $C_T = 2\pi r_{mean} C_{pul}$ represents total capacitance between the rings, where C_{pul} is the per unit length capacitance between the rings. The resonance frequency of SRR is given as f_{res}= $(L_{SRR}C_{SRR})^{-1/2}/2\pi$.

All the designs are simulated in three-dimensional COMSOL Multiphysics with the copper layer thickness less than skin depth in given frequency range. Thus, a Perfect electric conductor (PEC) is used to model this metallic copper layer and Perfect matched layers (PMLs) on the top and bottom are used to absorb all the port and higher order mode signal. The magnetic field, H_x is applied through interior source port 1 via a slit.The scattering boundary after the port 2 helps to scatter all the signal coming out of the SRR. The wavelength of $2\pi/\mid k_0 cos\theta \mid$ in the PML is dependent on the angle of incidence so that we can observe the variation characteristics of peak passbands and stop bands in transmission (S_{21}) and reflection (S_{11}). Finally, the periodic boundry condition is set to get identical 13×13 arrays of dielectric FSSs.

The transmission characteristics for different angles of incidence and various physical parameters like ring width and gap separation are analyzed with the applied external magnetic

field. The normalized electric field distribution and reflection/ transmission characteristics around 20 GHz are illustrated in Fig. 35 showing very good transmission response over the simulated frequency range. The maximum field is observed across the surface of the SRR compared to vicinity of the gap portion.

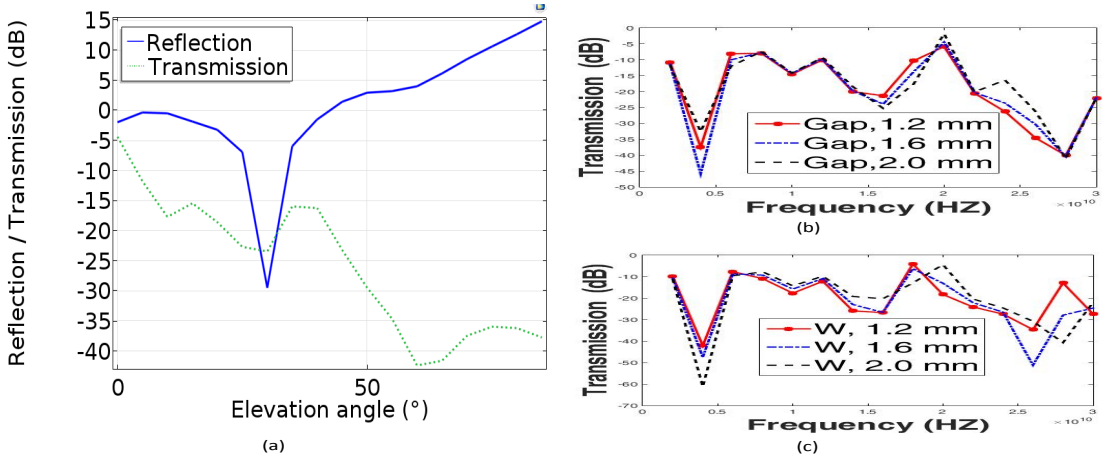

Figure 36: (a) Transmission and reflection characteristics as function of incident angle (b) Transmission characteristics as function of split gap seperation (c) Split ring width.

It is found that, the transmission of CSRR gradually decreases for increasing angle of incidence. Changes in the split gap and width dimension varies the capacitance. Changes in gap between inner and outer rings varies the inductance of the CSRR. Better transmission is obtained when both gap and width are increased, with slight change in resonance frequency, because of confinement of more field locally compared to free space due to refraction and diffraction phenomena. These characteristics are clearly shown in Fig. 36 which shows that increased number of cuts reduces the resonance frequency and gives better transmission due to increment in overall capacitance. Likewise, the resonance frequency is decreased for continuously rising dielectric constant of the substrate material as illustrated in Fig. 37.

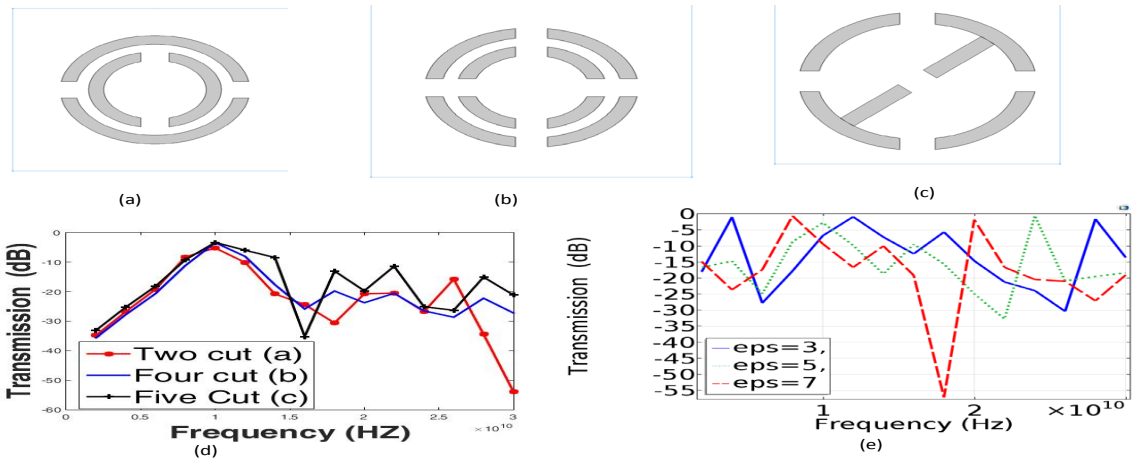

Figure 37: (a) CSRR with two cuts (b) CSRR with four cuts (c) Single ring with rectangular cut (d) The transmission characteristics for different (a,b and c) CSRR structure (e) Dependent of dielectric constant on transmission.

5.2 Metamaterial Inspired Antenna Design for Massive MIMO, 5G Communications System

Massive MIMO is an emerging technology for future wireless communication to provide higher spectral efficiency and data rate. This technology is the best candidate for 5G cellular systems due to reliable data link and better performance using hundreds of large antenna arrays in base stations. MIMO includes highly directed radiation beams through adaptive beam forming and signal processing algorithms for different pairs of antennas set. The thousands of user terminals are controlled using a full-dimensional MIMO scheme to reduce complexity/latency/interference using highly accurate channel state information (CSI) and simplified multiple access [88].

Several research investigations are made to address the size constraint within the large antenna array MIMO base station.The different test beds were designed using 64×64 antenna array operating at 2.4 GHz , and a 128×128 cylinderical array operating at 2.6 GHz for fewer number of users terminals. Recently, wireless mobile companies like Samsung

and AT&T also trying to implement such types of testbed for their users. Therefore, the meta-material based, miniature antenna design is popular in hyper MIMO communities. Hundreds of such sub-wavelength dimension antennas can be fabricated in periodic fashion to produce exotic electromagnetic behavior in the microwave and millimeter frequency bands. The highly directed beam forming signal can be achieved by actively controlling the individual voltage to each meta-material unit cell. Nathan et. all (2015) investigated the use of such reconfigurable holographic meta-material antennas for satellite communications. These holographic antenna provide sidelobe cancellation using active electronic scanning and produces an optimized far field radiation pattern.

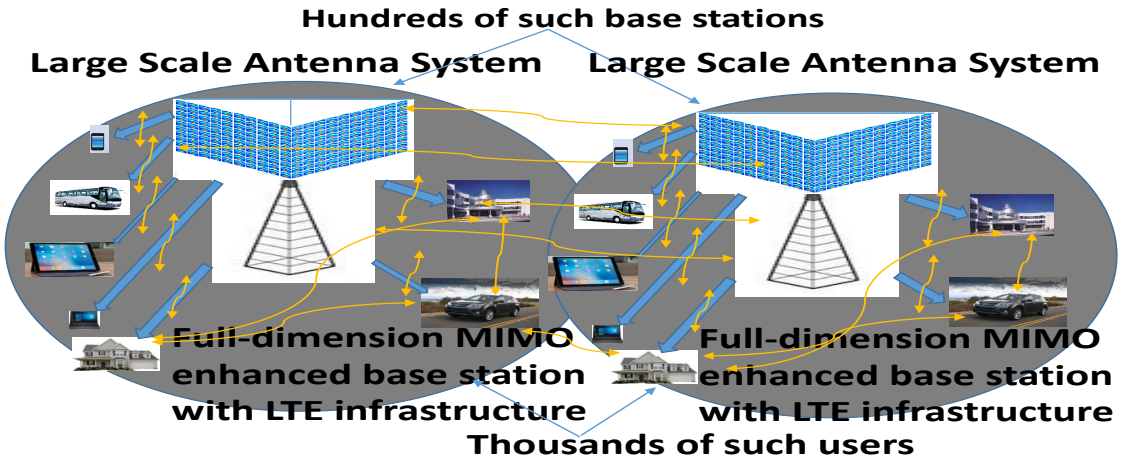

Figure 38: The general layout of massive MIMO architecture. It consist of Full-dimension MIMO enhanced base station with LTE infrastructure, very large antenna array, and thousands of user equipment.

The general layout for full dimension MIMO system is illustrated in Fig. 38. This includes enhanced node-B for Long term evolution (LTE) base stations, 3-D channel propagation model, multi user shared acess, software defined air interface, large number of base station antennas, user equipment (UE) for mobile terminal, and reference signal for pilot signal. We focus here on the study of very large antenna array system. This paper explores the design of such meta-material based antennas for masive MIMO communication operating at 1 GHz.

The unit cell has a simple inset feed patch structure to get a highly directed beam along a particular direction. The analysis of such structures will enable future studies on very large MIMO with channel correlation, diversity gain, mutual coupling, inter channel interference and other criteria [107] .

The meta-material inspired unit cell structure used for large array system operating at 11 GHz is shown in Fig. 39. It consists of an inset patch structure on a dielectric substrate layer. The Rogers RT5880 ($\epsilon = 2.2$) and RT5870 ($\epsilon = 2.33$) alternate layers can be used as dielectric substrates. These dielectric materials have very low loss and good electric properties over the desired frequency ranges. This simplest design produces a high-gain radiation pattern and can be fabricated within a communication printed circuit boards (PCB).

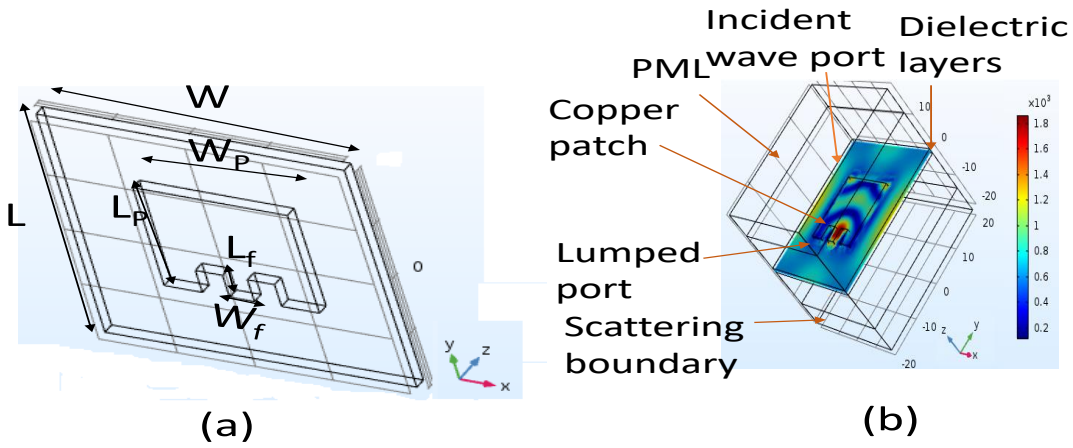

Figure 39: (a) Unit cell structure. W=L=40 , $W_P = 20, L_P = 18, W_f = 3.5$, and $L_f = 20$ mm (b) COMSOL design layout showing the electric field pattern.

The mutual coupling between many antennas is important to reduce the diversity factor in very large MIMO array. Antenna diversity performance can be evaluated to increase radiation efficiency of such array systems. The envelope correlation coefficient is defined as the average correlation between the total radiated power within 3-D space. The envelope correlation can be calculated from the S-parameters of the antenna as [108],

$$\rho_e = \frac{\mid S_{11}^* S_{12} + S_{21}^* S_{22} \mid}{(1 - (\mid S_{11} \mid^2 + \mid S_{21} \mid^2))(1 - (\mid S_{22} \mid^2 + \mid S_{12} \mid^2))} \tag{107}$$

The approximate diversity gain of MIMO antenna can be related to correlation coefficient as,

$$G_{app} = 10 \times \sqrt{1 - \mid \rho_e \mid} \tag{108}$$

All the designs are simulated in three dimensional COMSOL Multiphysics finite element analysis tool. The Perfect electric conductor (PEC) is used to model thin metallic antenna part. This is due to the small copper thickness compared to the skin depth. The lumped port is used in the antenna feed and the input signal is applied using port 1 via a slit.The Perfect matched layers (PMLs) on the top and bottom are used to absorb all the port and higher order mode signals. The scattering boundary helps to scatter all the signal coming out from the antenna unit. Finally, a Periodic boundary condition is set to get identical 10×10 arrays of such antennas.

The radiation characteristics for inset patch antenna as a meta-material unit cell for frequency ranges 9 GHz to 12 GHz are analyzed. The Fig. 39 shows electric field pattern near resonance of such a structure. Further, we create the model of 4×4 array of such unit cell as basic MIMO cell. The Fig. 40 shows the good resonance of such meta-material antennas array having S_{11} around -16 dB and low mutual coupling less than -10 dB. From this design, we found the highly directed beam patten with 6.88 dB gain along the direction of maximum radiation.

The Fig. 41 shows 3-D radiation pattern, azimuthal and elevation pattern for such antennas. Moreover, we can find the correlation coefficient and diversity gain using equation 107 and 108 for such antenna in order to analyse mutual coupling and interference between numbers of antenna arrays.

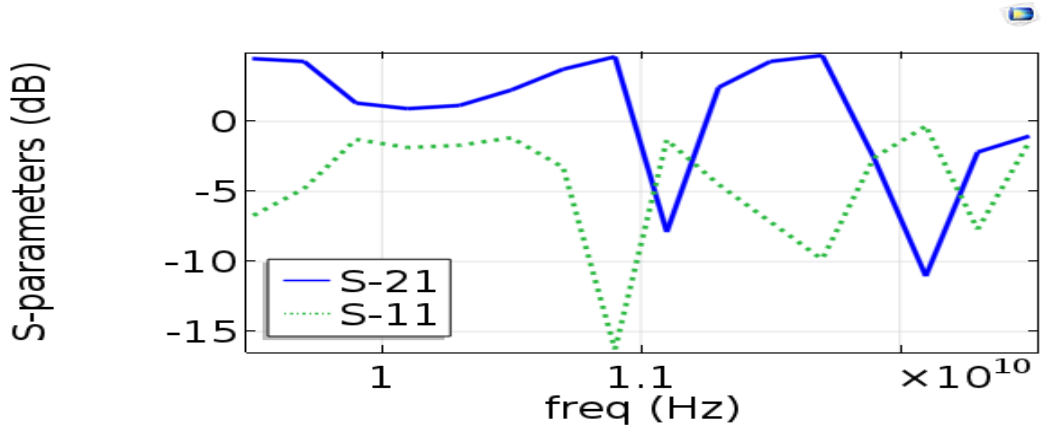

Figure 40: S parameters of 4×4 MIMO unit

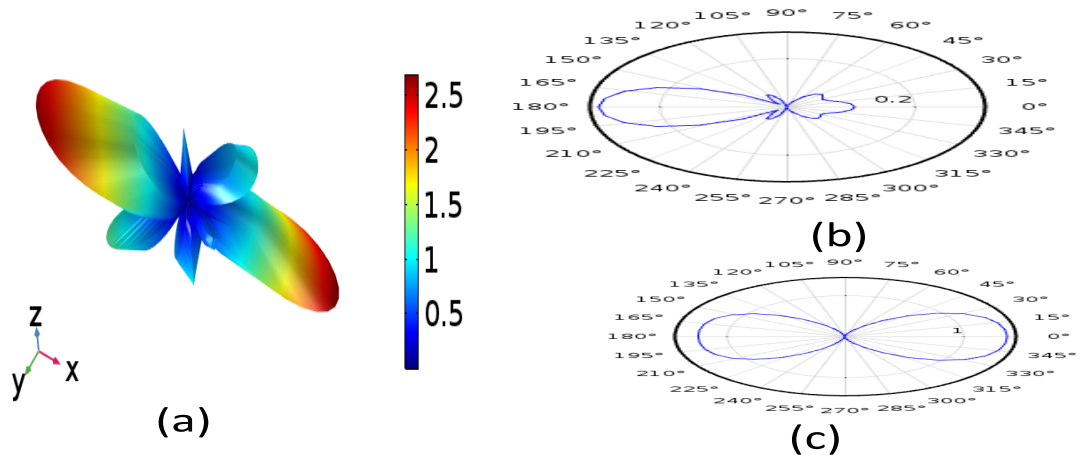

Figure 41: (a) The 3-D radiation pattern (b) Azimuth radiation pattern (c) Elevation radiation pattern for 4× 4 Massive MIMO array unit.

5.3 Summary

This chapter includes other related application of our research projects including frequency selective surfaces and metamaterial inspired antenna design for massive MIMO, 5G communications system. For frequency selective surfaces, we present the transmission characteristics of various SRR structures. By analyzing the SRR and CSSR with equivalent LC resonance circuits, we can change the magnetic resonance by altering physical parameters like dielectric constant, split width, and gap etc. We found that the increment on number of cuts and

dielectric constant in SRR reduces the frequency due to increase in overall capacitance. In second part, we presented the design of array antennas for use in massive MIMO wireless communication system. We discussed the overall architecture of full dimension MIMO used for next generation cellular technology. The meta-material inspired inset patch antenna solves the problem of size constraint, mutual coupling, channel correlation and produces a highly directed beam pattern.

CHAPTER 6

CONCLUSION AND FUTURE WORK

In conclusion, I explored the electromagnetic characteristics of dielectric multilayer structures and surface gratings each with a MLS profile. The MLS system is an aperiodic system that has been little studied for applications in optics. It is a system that is ripe for investigation as a means to support optical localization and surface waves, and as an ultra-wide photonic band gap material in two and three dimensions. The wide range of periodicities contained in an MLS structure leads to broadband reflection characteristics for all incident angles. Mainly, my dissertation is focused on the study of MLS multilayer structures that are equivalent to the perfect dielectric mirror and MLS Bloch surface wave excitation through MLS mediated grating coupling.

In the first part of my dissertation work, I examined the reflection performance of MLS multilayer structures at visible wavelengths. The analysis here shows that multilayers with an MLS profile can function as an effective omni-directional reflector. The narrow reflectivity dips mean that such reflectors would not be good for monochromatic laser reflection but rather for incoherent broad bandwidth light. The comparative analysis presented was made both to periodic multilayers and to the metallic reflectors silver and aluminum, whose refractive index was modeled based on the Brendel-Bormann (BB) model in the visible frequency region. I demonstrated broadband reflection for the MLS multilayer design by varying the number of layers or the refractive index of the constituent layers.

In the second part of the dissertation, I presented an exploration of the excitation of Bloch surface waves in dielectric multi-layers with MLS grating structures on the topmost layer. This MLS grating structure, an aperiodic system which contains a wide range of periodicities leading to broadband coupling of monochromatic light or wide spectral range of collimated light into Bloch surface waves on a periodic multilayer. The comparative analysis presented was made both to periodic and MLS grating profiles. Study results lead to the

possibility of more sensitive as well as broader Bloch surface wave coupling compared to a periodic grating counterpart. We conducted a detailed analysis of the surface electric field and angular sensitivity to better understand the characteristics of MLS grating coupling. The qualitative design and analysis of such aperiodic structures shows significant promise for future applications in optics and biosensors.

Further, in this thesis, we presented an analysis of frequency-selective-surface structure designs useful in metamaterial devices and 5G antenna applications. Specifically, we present transmission characteristics of various SRR structures. By analyzing the SRR and CSSR with equivalent LC resonance circuits, we can change the magnetic resonance by altering physical parameters like dielectric constant, split ring width, and gap etc. We found that the increment on number of cuts and dielectric constant in SRR reduces the frequency due to increase in overall capacitance. The good transmission ability of FSS is possible by increasing the gap and split width. The qualitative design and analysis of such structures will have application in negative index meta-materials, high resolution imaging, 5G antenna design, and RF device design. We also presented the design of antenna arrays for use in massive MIMO wireless communication system. We discussed the overall architecture of full dimension MIMO used for next generation cellular technology. The meta-material inspired inset patch antenna solves the problem of size constraint, mutual coupling, channel correlation and produces a highly directed beam pattern. The qualitative design and analysis of such antenna arrays will enable energy and spectrum efficient future wireless connectivity between thousands of users.

Finally, we discuss future directions of research interest in maximum length sequence multilayers and gratings. Key future goals involve improving the design of the multilayer platform, optimizing the performance of optical components, and projecting the contribution of this work to the evolution of further MLS multilayer reflector and grating BSWs for sensing and integrated optics applications. An important extension based on our MLS multilayer findings is the possibility of a complete band gap structure using a three-dimensional

maximum length sequence photonic crystal. Three-dimensional (3D) photonic crystal structures have potential applications in the fields of nanophotonics, sensing, cloaking, quantum electrodynamics control, and photometric conversion in solar cells. Various 3D photonic structures have been studied including Yablonovite, the woodpile structure, and the inverse opal. These photonic crystals consist of composite structures that are periodic.The effect of scattering and interference in such regular arrays leads to complete photonic band gaps permitting the control of light down to the single photon level by localizing the light in all three dimensions. We hypothesize that such deterministic aperiodic structures can produce much larger 3D photonic band gaps without the need of high index contrast.

BIBLIOGRAPHY

[1] M.Vishanathan,"*Simulation of digital communication systems using Matlab*," (Gaussian waves ISBN-9781301525089, 2013).

[2] M. Cohn and A. Lempe, "On Fast M-Sequence Transforms," IEEE Trans. on Inform. Th. **23**, 135-137 (1977).

[3] D.V. Sarwate and M.B. Pursley, "Cross correlation properties of pseudo random and related sequences," Proc. of IEEE **68** (5), 593 - 619 (1980).

[4] H. Jens,"Impulse response measurements using MLS," *PDF,Paper describing MLS generation. Contains C-code for MLS generation using up to 18-tap-LFSRs and matching Hadamard transform for impulse response extraction,*, `http://jenshee.dk/signalprocessing/mls.pdf`.

[5] P. Yeh, A. Yariv, and A. Y. Cho, "Optical surface waves in periodic layered media," Appl.Phys. Lett., **32**, no. 2, 104, (1978).

[6] M. Kness," ColorPy-A Python package for handling physical descriptions of color and light spectra", http://www.markkness.net/colorpy/ColorPy.html ,(2008).

[7] W. M. Robertson, "Experimental Measurement of the Effect of Termination on Surface Electromagnetic Waves in One-Dimensional Photonic Bandgap Arrays," J. Lightwave Technol. **17**, 2013-2017 (1999).

[8] M. Shinn and W. M. Robertson, "Surface plasmon-like sensor based on surface electromagnetic waves in a photonic band-gap material," Sensors and Actuators B: Chemical, **105**, 2, 360-364 (2005).

[9] T. Kovalevich, P. Boyer, M. Suarez, R. Salut, M.-S. Kim, H. P. Herzig, and M. P. Bernal, "Polarization controlled directional propagation of Bloch surface wave," Opt. Express **25**, 5710–5715 (2017).

[10] M. Liscidini, and J. E. Sipe, "Enhancement of diffraction for biosensing applications via Bloch surface waves," *Appl. Phys. Lett.*, **91**, 253125 (2007).

[11] S. Pirotta, X. G. Xu, A. Delfan, S. Mysore, S. Maiti, G. Dacarro, M. Patrini, M. Galli, G. Guizzetti, D. Bajoni, J. E. Sipe, G. C. Walker, and M. Liscidini, "Surface-enhanced Raman scattering in purely dielectric structures via Bloch surface waves," *J. Phys. Chem. C*, **117**, 6821 – 6825 (2013).

[12] M. Scaravilli, A. Micco, G. Castaldi, G. Coppola, M. Gioffrè, M. Iodice, V. La Ferrara, V. Galdi, A. Cusano,"Excitation of Bloch Surface Waves on an Optical Fiber Tip,"*Advanced Optical Materials* ,**6**, 1800477, 2018.

[13] V. Koju, and W. M. Robertson,"Leaky Bloch-like surface waves in the radiation-continuum for sensitivity enhanced biosensors via azimuthal interrogation. Sci Rep **7**, 3233 (2017).

[14] Kuon Inoue, Hisaya Oda, Naoki Ikeda, and Kiyoshi Asakawa, "Enhanced third-order nonlinear effects in slowlight photonic-crystal slab waveguides of linedefect," Opt. Express **17**, 7206-7216 (2009).

[15] F Frascella, S Ricciardi, L Pasquardini, C Potrich, A Angelini, A Chiadò, C Pederzolli, N De Leo, P Rivolo, C F Pirri, E Descrovi,"Enhanced fluorescence detection of miRNA-16 on a photonic crystal",*The Royal Society of Chemistry*, **140**, 5459-5463 (2015).

[16] Roussey, Matthieu,"Slot Waveguide Enhanced Bloch Surface Waves",*Applied Sciences*, **18**, 5459-5463 (2018).

[17] X. Kang, H. Lu, and Z. Wang, "Guided Bloch surface wave resonance by near normal and near in-plane illuminations: the hyper azimuthal sensitivity," Opt. Express **26**, 12769-12778 (2018).

[18] Y. Li, and T. Yang, S. Song, and Z. Pang, G. Du, and S. Han,"Phase properties of Bloch surface waves and their sensing applications",*Appl. Phys. Lett.*, **103**, 041116 (2013).

[19] W. P. Guidorzi, L. Barbaresi, D. D′Orazio, M. Garai, "Impulse Responses Measured with MLS or Swept-Sine Signals Applied to Architectural Acoustics: An In-depth Analysis of the Two Methods and Some Case Studies of Measurements Inside Theaters," Energy Procedia **78**, 1611-1616, (2015).

[20] K. N. Poudel and S. Gangaju, "Spectral Efficiency, Diversity Gain and Multiplexing Capacity Analysis for Massive MIMO, 5G Communications System," *Int.Conf. on Net. and Net.Appl. doi: 10.1109/NaNA.2017.45*, 133-137 (2017).

[21] W. T. Chu, "Impulse-response and reverberation-decay measurements made by using a periodic pseudorandom sequence," Appl. Acous. **29**, 193-205, (1990).

[22] S.W. Golomb, "Spread Spectrum Techniques and Applications," *IEEE, Third Intl. Symposium on Spread Spectrum Techniques and Application*, (1994).

[23] J. R. Devore, "Refractive Indices of Rutile and Sphalerite," J. Opt. Soc. Am. A **41**, 416 (1951).

[24] T. Siefke, S. Kroker, K. Pfeiffer, O. Puffky, K. Dietrich, D. Franta, I. Ohlídal, A. Szeghalmi, E.-B. Kley, A. Tunnermann, "Materials Pushing the Application Limits of Wire Grid Polarizers further into the Deep Ultraviolet Spectral Range," Adv. Optical Mater. **4**, 1780 (2016).

[25] Rei Kitamura, Laurent Pilon, and Miroslaw Jonasz, "Optical constants of silica glass from extreme ultraviolet to far infrared at near room temperature," Appl. Opt. **46**, 8118-8133 (2007)

[26] S. J. Orfanidis, "Electromagnetic Waves and Antennas, online book," ,`https://www.ece.rutgers.edu/~orfanidi/ewa/`,**1**, 1413 (2016).

[27] J. Lekner, "Omnidirectional reflection by multilayer dielectric mirrors," *J. Opt. Pure. Appl.*, **2**, 349-352 (2000).

[28] K.R. Harper,"Theory, Design, and Fabrication of Diffractive Grating Coupler for Slab Waveguide"Brigham Young University - Provo,2003

[29] D. Rosenblatt and A. Sharon and A. A. Friesem, "Resonant grating waveguide structures," *IEEE Journal of Quantum Electronics*, **33**, 2038-2059 (1997).

[30] Khem Narayan Poudel and William M. Robertson, "Maximum length sequence dielectric multilayer reflector," OSA Continuum 1, 358-372 (2018).

[31] K.N. Poudel, V.Koju and W. M. Robertson, "Maximum length sequence (MLS) multilayer reflector using rigorous coupled wave analysis and FEM," 2018 USNC-URSI Radio Science Meeting (Joint with AP-S Symposium, (2018).

[32] M. Bernier, F. Garet, and J. Coutaz, Precise Determination of the Refractive Index of Samples Showing Low Transmission Bands by THz Time-Domain Spectroscopy*IEEE Trans.on THz Sci. and Tech.*, vol. 3, no. 3, pp. 295-301, May. 2013.

[33] KN Poudel, V Koju, W Robertson,"Frequency selective surfaces for microwave frequency band applications", - USNC-URSI Radio Science Meeting (Joint with AP-S, 2017).

[34] Yi-nan Li, Jian Li, Zhou-mo Zeng, Jie Li, Zhen Tian, and Wei-kui Wang, "Terahertz spectroscopy for quantifying refined oil mixtures," Appl. Opt. 51, 5885-5889 (2012).

[35] M. G. Moharam, E. B. Grann,T. K. Gaylord, and D. A. Pommet, "Formulation for stable and efficient implementation of the rigorous coupled-wave analysis of binary gratings," *J. Opt. Soc. Am. A*, **12**, 1068 – 1076 (1995).

[36] P. Lalanne and E. Silberstein, "Fourier-modal methods applied to waveguide computational problems," *J. Opt. Lett.* , **25**, 1092 – 1094 (2000).

[37] R. C. Rumpf, "Improved formulation of scattering matrices for semi-analytical methods that is consistent with convention," *Progress In Electromagnetics Research B*, **35**, 241 – 261 (2011).

[38] L. Li, "Formulation and comparison of two recursive matrix algorithms for modeling layered diffraction gratings," *J. Opt. Soc. Am. A*, **13**, 1024-1035 (1996).

[39] V.Koju , " Computational modelling of bloch surface waves in one dimensional periodic and aperiodic multilayer structure ," PHD thesis, Middle Tennessee State University (2017).

[40] Matthew N. O. Sadiku. 2009. Numerical Techniques in Electromagnetics with Matlab, Third Edition (3rd ed.). CRC Press, Inc., Boca Raton, FL, USA.

[41] *https* : *//en.wikipedia.org/wiki/COMSOLMultiphysics.*

[42] LN Acquaroli Matrix method for thin film optics- arXiv preprint arXiv:1809.07708, 2018 - arxiv.org.

[43] *https* : *//www.ifm.liu.se/courses/TFYY*67*/Lect*13*.pdf*

[44] Bo E. Sernelius, 'Surface Modes in Physics', Wiley-VCH, Berlin 2001.

[45] E. Liu , " EMpy - ElectroMagnetic Python, "Formulation for stable and efficient implementation of the rigorous coupled-wave analysis,of binary gratings", (2009).

[46] Bolla, L. (2017). EMpy [Computer software]. https://github.com/lbolla/EMpy/

[47] M. G. Moharam, E. B. Grann,T. K. Gaylord, and D. A. Pommet, "Stable implementation of the rigorous coupled-wave analysis for surface-relief gratings: enhanced transmittance matrix approach," *J. Opt. Soc. Am. A*, **12**, 1077 – 1086 (1995).

[48] P. Lalanne and G. M. Morris, "Highly improved convergence of the coupled-wave method for TM polarization," *J. Opt. Lett.* , **13**, 779 – 784 (1996).

[49] L. Zhang, " RicWaA - Rigorous Coupled Wave Analysis (RCWA),project of Deng Research Group at Physics Department of University of Michigan." (2010).

[50] A. C. Polycarpou, " Introduction to the Finite Element Method in Electromagnetics.,Synthesis Lectures on Computational Electromagnetics", **1**, 1 – 126 (2005).

[51] J.M. Jin, The Finite Element Method in Electromagnetics,John Wiley and Sons, Inc., New York, 1993.

[52] $https : //www.comsol.com/blogs/simulation - tools - for - solving - wave - electromagnetics - problems/$

[53] A. C. Cangellaris, "Frequency-domain finite element methods for electromagnetic field simulation: fundamentals, state of the art, and applications to EMI/EMC analysis," Proceedings of Symposium on Electromagnetic Compatibility, Santa Clara, CA, USA, 107-116, (1996).

[54] H. Whitney,"Geometric Integration Theory", Princeton Mathematical Series, **21**, Princeton, NJ and London: Princeton University Press and Oxford University Press, XV+387,(1957)

[55] J.C. Nedelec, "Mixed finite elements in R3," Numerical Math-cmatics, **35**, 315-341, (1980)

[56] G. Mur, "Finite-element modeling of three-dimensional time- harmonic electromagnetic fields in inhomogeneous media," Ra- dio Science, **26**, 275-280, (1991)

[57] R. Brendel and D. Bormann, "An infrared dielectric function model for amorphous solids," J. Appl. Phys. **71**, 11-61992, (1992).

[58] M. Abramowitz and I. A. Stegun, eds., Handbook of Mathematical Functions, Dover, New York 1972.

[59] H. A. Macleod, Thin-Film Optical Filters Adam Hilger, Bristol, UK, 1986.

[60] Z. Knittl, Optics of Thin Films Wiley,New York, 1976

[61] M. I. Markovic and A. D. Rakic , "Determination of optical properties of aluminum including electron reradiation in the Lorentz–Drude model," Opt. Laser Technol. **22**, 394 –398, (1990)

[62] $https://my.ece.utah.edu/\ ece6340/LECTURES/lecture/2014/FDTD.pdf$.

[63] A. Taflove, S. C. Hagness, Computational Electrodynamics: The Finite-Difference Time-Domain Method, Norwell, MA, USA:Artech House, 2005.

[64] A. Taflove, A. Oskooi, and S.G. Johnson, Advances in FDTD Computational Electrodynamics: Photonics and Nanotechnology, Artech: Norwood, MA, 2013.

[65] Kane Yee. "Numerical solution of initial boundary value problems involving Maxwell's equations in isotropic media". IEEE Transactions on Antennas and Propagation. **14** 302–307, (1966).

[66] S. Kong, J. J. Simpson and V. Backman, "ADE-FDTD Scattered-Field Formulation for Dispersive Materials," in IEEE Microwave and Wireless Components Letters, **18**, 4-6, (2008.

[67] $https://meep.readthedocs.io/en/latest/Yee_Lattice/$

[68] $http://drjamesnagel.com/notes/Nagel20-20FDTD_Introduction.pdf$

[69] F.I. Baida, A. Belkhir. Finite Difference Time Domain Method For Grating Structures. E. Popov. Gratings: Theory and Numeric Applications, AMU (PUP), 9.1-9.36, (2012)

[70] R. Courant, K. O. Friedrich, and H. Lewy. On the partial difference equations of mathematical physics. IBM Journal of Research and Development, **11**,215–234, (1967).

[71] Ardavan F. Oskooi, David Roundy, Mihai Ibanescu, Peter Bermel, J.D. Joannopoulos, Steven G. Johnson, Meep: A flexible free-software package for electromagnetic simulations by the FDTD method, Computer Physics Communications, **181**, 3,

, 687-702, (2010).

[72] Y. Fink, J. N. Winn, S. Fan, C. Chen, J. Michel, J. D. Joannopoulos, E. L. Thomas, "A Dielectric Omnidirectional Reflector," Science **282**, 1679 (1998).

[73] B. Gallas, S. Fisson, E. Charron, A. B. Bruneau, G. Vuye, and J. Rivory, "Making an omnidirectional reflector," Appl. Opt. **40**, 5056-5063 (2001).

[74] A. Rakic, A. Djurisic, J. Elazar, and M. Majewski, "Optical properties of metallic films for vertical-cavity optoelectronic devices," Appl. Opt. **37**, 5271-5283 (1998).

[75] M. Schroeder, "Diffuse sound reflection by maximum-length sequences," J. Acoust. Soc. Am. **57** 149-150, (1975).

[76] J. Xu, H. Fang, and Z. Lin, "Expanding high reflection range in a dielectric multilayer reflector by disorder and inhomogeneity," J. Phy. D:Appl Phy. **34**, 445-449 (2001).

[77] J. Xu, H. Fang, and Z. Lin, "Broadband optical reflector-an application of light localization in one dimension," Appl. Phy. Lett. **67**, 2431-2432 (1995).

[78] L. Li, J. A. Dobrowolski, M. Jacobson, C. Cooksey, "Broadband transmission filters from the 2013 Optical Interference Coatings manufacturing problem contest," Appl. Opt. **53** A248 (2014).

[79] V. Koju and W. M. Robertson, "Excitation of Bloch-like surface waves in quasi-crystals and aperiodic dielectric multilayers," Opt. Lett. **41**, 2915-2918 (2016).

[80] D. L. Negro and S.V. Boriskina, "Simulation methods for multiperiodic and aperiodic nanostructured dielectric waveguides. Deterministic aperiodic nanostructures for photonics and plasmonics applications," Laser Photonics Rev. **6** (2), 178-218 (2012).

[81] Z. V. Vardeny, A. Nahata, and A. Agrawal, "Optics of photonic quasicrystals," Nat. Phot. **7** , 117 (2013).

[82] N. H. Liu, "Propagation of light waves in Thue-Morse dielectric multilayers," Phys. Rev. B **B 55** 3543-3547, (1997).

[83] M. Dulea, M. Johansson, and R. Riklund, "Localization of electrons and electromagnetic waves in a deterministic aperiodic system," Phys. Rev. **B 45**, 105-114 (1992).

[84] M. Paulsen, L. T. Neustock, S. Jahns, J. Adam, and M. Gerken, "Simulation methods for multiperiodic and aperiodic nanostructured dielectric waveguides," Opt Quant Electron. **49**, 107 (2017).

[85] M. Kohmoto, L. P. Kadanoff, and C. Tang, "Localization Problem in One Dimension: Mapping and Escape," Phys. Rev. Lett. **50**, 1870 (1983).

[86] R. Nava, J. T. Martinez, J. A. D. Rio, and G. G. Naumis, "Perfect light transmission in Fibonacci arrays of dielectric multilayers," J. Phys.Condens. Matter **21**, 155901 (2009).

[87] M. P. Van Albada and A. Lagendijk,"Observation of weak localization of light in a random medium," Phys. Rev. Lett. **55**, 2692-2695 (1985).

[88] K. N. Poudel, D. Schurig and N. Patwari, "Spatial imaging using a communication system's channel state information," in *2016 USNC-URSI Radio Science Meeting,* 41–42, (2016).

[89] K. N. Poudel and W. Robertson, "Metamaterial inspired antenna design for massive MIMO, 5G communications system," in *2017 USNC-URSI Radio Science Meeting (Joint with AP-S Symposium),* USA, 103–104, (2017).

[90] K. N. Poudel and V. Koju and W. Robertson, "Frequency selective surfaces for microwave frequency band applications," in *2017 USNC-URSI Radio Science Meeting (Joint with AP-S Symposium,* USA, 15–16, (2017).

[91] K. N. Poudel and W. M. Robertson, "Bloch surface wave excitation using a maximum length sequence grating structure," in *SPIE OPTO, the optoelectronics, photonic materials and devices conference,* San Francisco, CA, USA, 10914, (2019)

[92] Ľ. Scholtz, L. Ladanyi and J. Müllerová, Advances in Electrical and Electronic Engineering, **12**, 631, (2014)

[93] J. R. Devore, "Refractive indices of rutile and sphalerite," J. Opt. Soc. Am. A **41**, 416–419 (1951).

[94] I. H. Malitson, "Interspecimen comparison of the refractive index of fused silica," J. Opt. Soc. Am. A **55**, 1205–1209 (1965)

[95] M. Cohn and A. Lempe, "On Fast M-Sequence Transforms," IEEE Trans. on Inform. Th. **23**, 135-137 (1977).

[96] A. Sinibaldi, R. Rizzo, G. Figliozzi, E. Descrovi, N. Danz, P. Munzert, A. Anopchenko, and F. Michelotti, "A full ellipsometric approach to optical sensing with Bloch surface waves on photonic crystals," Opt. Express **21**, 23331–23344 (2013).

[97] Z. Cheng, R. Savit, and R. Merlin, "Structure and electronic properties of Thue-Morse lattices," Phys. Rev.B **375**, 4375-4382 (1988).

[98] E. Macia, "Exploiting aperiodic designs in nanophotonic devices," Rep. Prog. Phys. **75**, 036502(2012).

[99] M. Kohmoto, B. Sutherland, and K. Iguchi, "Localization of optics: Quasiperiodic media," Phys. Rev. Lett. **58**, 2436-2438 (1987).

[100] M. Kohmoto, B. Sutherland, and K. Iguchi, "Localization of light waves in Fibonacci dielectric multilayers," Phys. Rev. Lett. **72**, 633-636 (1994).

[101] L. D. Negro, N. Feng, and A. Gopinath, "Electromagnetic coupling and plasmon localization in deterministic aperiodic arrays," J. Opt. A. **10**, 064013 8 (2008).

[102] K. N. Poudel, V. Koju, and W. Robertson,"Maximum Length Sequence (MLS) Multilayer Reflector using Rigorous Coupled Wave Analysis and FEM,"presented at the IEEE USNC-URSI Radio Science Meeting Joint with AP-S, Boston, USA,7-14 (2018).

[103] J. D. Baena et al., "Equivalent-circuit models for split-ring resonators and complementary split-ring resonators coupled to planar transmission lines," in IEEE Transactions on Microwave Theory and Techniques, **53**, 4, 1451-1461, (2005).

[104] W. M. Robertson, G. Arjavalingam, R. D. Meade, K. D. Brommer, A. M. Rappe, and J. D. Joannopoulos,"Measurement of photonic band structure in a two-dimensional periodic dielectric array", Phys. Rev. Lett.**68**, 2023 (1992).

[105] J. B. Pendry, A. J. Holden, D. J. Robbins and W. J. Stewart, "Magnetism from conductors and enhanced nonlinear phenomena," in IEEE Transactions on Microwave Theory and Techniques, vol. **47**, 11, 2075-2084, (1999).

[106] D. R. Smith and D. Schurig, "Electromagnetic Wave Propagation in Media with Indefinite Permittivity and Permeability Tensors," Phys. Rev. Lett. **90**, 077405 (2003).

[107] E. G. Larsson, O. Edfors, F. Tufvesson and T. L. Marzetta, "Massive MIMO for next generation wireless systems," in IEEE Communications Magazine, **52**, 186-195, (2014).

[108] S. Blanch, J. Romeu and I. Corbella, "Exact representation of antenna system diversity performance from input parameter description," in Electronics Letters, **39**, 705-707, (2003).

[109] M. Queff elec, Substitution dynamical systems-spectral analysis (Springer Verlag, Berlin, 2010)